## Title

Activation and expansion of presynaptic signaling foci drives presynaptic homeostatic plasticity.

## Permalink

https://escholarship.org/uc/item/3r23z7zj

## Journal

Neuron, 110(22)

## Authors

Orr, Brian
Fetter, Richard
Davis, Graeme

## Publication Date

2022-11-16

## DOI

10.1016/j.neuron.2022.08.016

Published in final edited form as:
*Neuron*. 2022 November 16; 110(22): 3743–3759.e6. doi:10.1016/j.neuron.2022.08.016.

# Activation and Expansion of Presynaptic Signaling Foci Drives Presynaptic Homeostatic Plasticity

**Brian O. Orr**,
**Richard D. Fetter**,
**Graeme W. Davis**
Department of Biochemistry and Biophysics, Kavli Institute for Fundamental Neuroscience, University of California, San Francisco, CA 94941

## SUMMARY

Presynaptic homeostatic plasticity (PHP) adaptively regulates synaptic transmission in health and disease. Despite identification of numerous genes that are essential for PHP, we lack a dynamic framework to explain how PHP is initiated, potentiated and limited to achieve precise control of vesicle fusion. Here, utilizing both mouse and *Drosophila*, we demonstrate that PHP progresses through the assembly and physical expansion of presynaptic signaling foci where activated Integrins biochemically converge with trans-synaptic Semaphorin2b/PlexinB signaling. Each component of the identified signaling complexes, including alpha/beta-Integrin, Semaphorin2b, PlexinB, Talin and Focal Adhesion Kinase (FAK), and their biochemical interactions, are essential for PHP. Complex integrity requires the Sema2b ligand and complex expansion includes a ~5-fold expansion of active-zone associated puncta composed of the actin-binding protein Talin. Finally, complex pre-expansion is sufficient to accelerate the rate and extent of PHP. A working model is proposed incorporating signal convergence with dynamic molecular assemblies that instruct PHP.

## INTRODUCTION

Homeostatic plasticity (HP) encompasses a suite of adaptive physiological processes that counteract disease-related neuronal perturbations, effectively representing a biochemical mechanism of brain resilience. Indeed, HP has been hypothesized to be intertwined with the pathophysiology of numerous neurological and psychiatric disorders including epilepsy, autism, ALS and Alzheimer's (Dickman & Davis, 2009; Frere & Slutsky, 2018; Genç et al., 2020; Mullins et al., 2016; Orr et al., 2020; Plomp et al., 1992). A particularly

---

**Corresponding author / Lead Contact:** Graeme Davis, Graeme.davis@UCSF.edu.

AUTHOR CONTRIBUTIONS
B.O.O, project design, data collection, data analysis, interpretation, co-writing and editing manuscript; R.D.F electron microscopy data collection, data analysis, interpretation; G.W.D., funding acquisition, project design, data interpretation, writing and editing manuscript.

DECLARATION OF INTERESTS
Graeme W. Davis is a member of the Advisory Board of the journal Neuron. The authors declare no other competing interests.

well-characterized form of HP regulates the release of neurotransmitter from presynaptic terminals, termed ‘presynaptic homeostatic plasticity’ (PHP). PHP has been documented at both peripheral and central synapses, in systems ranging from insects to human (Davis, 2006; Delvendahl et al., 2019; Frank et al., 2006; Plomp et al., 1992). Numerous genes have been defined as being necessary for PHP, identified through large-scale forward genetic screens in *Drosophila* (Brusich et al., 2015; Davis, 2013; Delvendahl & Müller, 2019; Dickman & Davis, 2009; Younger et al., 2013). Yet, in nearly every instance, identified genes have only been defined as genetically necessary. There is a paucity of information about how individual signaling elements are organized into coherent, dynamical signaling systems capable of detecting a perturbation and executing a homeostatic response that is both rapid and accurate, without evidence of oscillation or over-compensation Thus, despite evidence that homeostatic plasticity can be disease modifying, we lack essential mechanistic information that might, one day, be useful for manipulating homeostatic plasticity for therapeutic value. Here, we address this topic by defining a dynamical, homeostatic signaling system that occurs at the intersection of integrin-mediated signaling foci and trans-synaptic semaphoring/plexin signaling.

Semaphorin signaling is pervasive during neural development, controlling cell migration, growth cone guidance, synapse formation and dendrite outgrowth (Carulli et al., 2021; Yu & Kolodkin, 1999). Semaphorins and their receptors remain expressed in the adult brain and their removal is associated with epilepsy and autism (Carulli et al., 2021). We recently demonstrated that Semaphorin2b (Sema2b) functions as a retrograde, trans-synaptic signal necessary for PHP in *Drosophila* (Orr et al., 2017). However, while Sema2b signaling is necessary, it is not sufficient to modify baseline neurotransmitter release or PHP (Orr et al., 2017). It seems that another signaling system must also be engaged.

Integrin-mediated focal adhesions complexes (FAC) are among the most well-characterized signaling events during organismal development. FACs are dynamic, multi-protein assemblies that rapidly grow and shrink, thereby engaging and releasing adhesive force during cell migration and process outgrowth (Klapholz & Brown, 2017; Michael & Parsons, 2020; Schlaepfer et al., 1999). More recently, it has become apparent that integrins can also activate and shape other intercellular signaling events, with important implications for inflammation and cancer (Munger & Sheppard, 2011).

Within the nervous system, integrins have been demonstrated to control developmental dynamics including cell migration, growth cone motility and guidance, dendrite elaboration and synaptogenesis, generally functioning as dynamic mediators of intercellular adhesion and force transduction (Park & Goda, 2016). By contrast, the view of integrin function at synaptic connections in the mature nervous system is comparatively static with important roles in learning-related plasticity (Babayan et al., 2012; Park & Goda, 2016; Roman & Davis, 2001; Chan et al., 2006; Cingolani et al., 2008; Lin et al., 2003). Yet, the means by which integrins participate in synaptic plasticity remains uncertain. Is intercellular adhesion or force transduction required? How is integrin signaling regulated? Here, we provide evidence that Semaphorin and integrin signaling converge at the presynaptic plasma membrane, instructing the physical expansion of focal signaling assemblies that drive the induction and expression of PHP.

# RESULTS

## ITGB1 is necessary for PHP at the mouse NMJ.

Beta1-Integrin (ITGB1) is present at the mouse NMJ (Figure 1A–C) (Nishimune et al., 2008), is highly expressed in motoneurons (Schwander et al., 2004) and is enriched at intercellular junctions (Hall et al., 1990; Raghavan et al., 2000). Mechanistically, a general model of integrin activation suggests that ligand binding to a closed, bent conformation of alpha- and beta-Integrin heterodimers induces extension of the extracellular domains followed by separation of the cytoplasmic tails for full signaling potency (Figure 1D) (Michael & Parsons, 2020).

Presynaptic homeostatic plasticity (PHP) can be rapidly induced at the NMJ by application of sub-blocking concentrations (0.1μM) of the acetylcholine receptor (AChR) antagonist, curarine (Orr et al., 2020; Wang et al., 2016). Under control conditions, application of curarine rapidly (seconds) reduces the average amplitude of spontaneous miniature end plate potentials (mEPP). Evoked end plate potentials (EPP) are initially depressed but recover to baseline values due to an increase in presynaptic vesicle release, determined by calculating presynaptic quantal content (QC; see methods), (Figure 1E, F control; See also Supplemental Figure 1).

To test a role for ITGB1 during PHP, we turned to well-established tools that enable acute, pharmacological disruption of ITGB1 function (Figure 1D, reagents). Pre-incubation of the diaphragm NMJ (1–2hrs) with either of two ITGB1 function-blocking antibodies (AIIB2 and 9EG7; (Hall et al., 1990; Lenter et al., 1993)) completely eliminates the subsequent induction of PHP (Figure 1E, F). We confirmed this effect with a third reagent, pre-incubating the NMJ in RGD peptide, an inhibitor of integrin-ligand interactions (Park & Goda, 2016). Again, PHP expression was strongly suppressed (Figure 1F; p<0.01). The lack of a complete block with the RGD peptide could be attributed to many factors including incomplete tissue penetrance or less efficient target binding (see also Supplemental Figure 1).

Next, we extended our analysis to the homeostatic potentiation of the readily releasable synaptic vesicle pool (RRP) (Müller et al., 2015; Ortega et al., 2018; see methods). First, PHP was induced by application of curarine and a homeostatic potentiation of the RRP was documented. Next, we incubated the NMJ in AIIB2 and observed a complete reversal of previously induced homeostatic expansion of the RRP (Figure 1G, H). We note that AIIB2 antibody incubation does not reduce mEPC amplitude beyond the effects of curarine alone, yet strongly diminishes EPSC amplitude (Fig. 1H), an effect that is consistent with a block of PHP. Thus, it appears that ITGB1 signaling has a function that is necessary for PHP expression and maintenance.

Next, we turned to the genetic manipulation of ITGB1. We acquired a floxed allele of the *ITGB1* gene (Raghavan et al., 2000) and generated animals lacking *ITGB1* expression selectively in motoneurons ($ITGB1^{flox/flox}$, $HB9^{CRE/+}$). Animals are born in normal Mendelian ratios, are of normal weight and appear physically normal (Figure 2A, B). Visual inspection (P90) reveals that the diaphragm NMJ forms normally and baseline neurotransmission is indistinguishable from littermate controls (*ITGB1*$^{flox/flox}$) (Figure 2C, D; p>0.6, ANOVA with Tukey correction for multiple comparisons). Immunostaining with the presynaptic active zone marker Bassoon shows no difference comparing mutants to controls (Figure 2F) and there is no change in postsynaptic acetylcholine receptor distributions (Figure 2F) despite the loss of ITGB1 staining at the NMJ endplate (Figure 2G; synaptic ITGB1, defined as staining that resides within the circumference of AChR fields, reduced by ~95% compared to controls, p=0.001). With this as background, we demonstrate that PHP is completely blocked at NMJs that lack presynaptic ITGB1 (Figure 2D, E). The block of PHP is underscored by plotting the relationship of mEPP amplitude to quantal content (Figure 2E).

## ITGB1 is activated and re-localizes during PHP

The 9EG7 antibody preferentially binds to activated ITGB1 (Byron et al., 2009), allowing us to determine whether ITGB1 signaling is activated during PHP versus simply being persistently required. Under baseline conditions, immunostaining with the 9EG7 antibody shows limited direct overlap with AChR fields at the endplate (Figure 2G, control minus curarine 9EG7 staining). However, following induction of PHP (1hr curarine pre-incubation of the diaphragm NMJ), 9EG7 staining is significantly transformed into a ribbon-like distribution that precisely aligns with ridges of clustered postsynaptic AChRs (Figure 2G, control plus curarine, and insets as indicated). Importantly, the 9EG7 staining is abolished following genetic removal of ITGB1 from motoneurons (Figure 2G, top right panels, cKO minus/plus curarine). Finally, assessed total ITGB1 staining, assessed using the AIIB2 antibody, in the absence and presence of curarine. The AIIB2 staining shows a trend toward larger values following curarine incubation, but the effect is not statistically significant (Supplemental Figure 1D). Thus, the dramatic change in activated ITGB1, following curarine incubation, cannot be due to a major redistribution of total ITGB1 at the endplate. In order to further interrogate how integrin signaling participates in PHP, we turned to *Drosophila.*

## Presynaptic integrin signaling is necessary for PHP at the Drosophila NMJ.

In *Drosophila*, an ITGB1 orthologue encoded by the *myospheriod* (*mys*) gene is present at the larval NMJ (Beumer et al., 1999; Rohrbough et al., 2000). We used CRISPR-mediated gene editing to insert a GFP coding exon into the endogenous *mys* locus. At low magnification, Mys-GFP is concentrated to the NMJ where it co-localizes with anti-Mys immunostaining (Figure 3A, right top panels; see Supplemental Figure 2F for quantification). When imaged using super-resolution, structured illumination microscopy (SIM), Mys-GFP is observed to localize at the NMJ with a clear postsynaptic concentration within the muscle membranes of the sub-synaptic reticulum (SSR) (Figure 3A, white solid triangle). Analysis of single confocal planes that bisect the volume of presynaptic boutons reveals that Mys-GFP puncta also co-localize with a marker of the presynaptic plasma membrane (Figure 3A arrowheads; see also Supplemental Figure 2C), with some puncta being completely circumscribed by the presynaptic membrane. These observations are consistent with prior immuno-EM revealing presynaptic Mys protein aggregates in *Drosophila* boutons (Beumer et al., 1999). Finally, we confirm that a Flag-tagged Mys protein traffics to the presynaptic terminal when expressed in motoneurons (Figure 3A, right, bottom panel and inset).

At the *Drosophila* NMJ, PHP can be induced by application of the glutamate receptor antagonist philanthotoxin (PhTx, 15µM) (Frank et al., 2006; Genç & Davis, 2019). In control animals, PhTx reduces mEPP amplitude by ~50% and induces a compensatory, homeostatic increase in presynaptic quantal content (QC) that restores EPP amplitudes to baseline (Figure 3B, C; Supplemental Figure 2A). From here forward, data in primary figures are generally presented as percent change, comparing measurements made in the presence versus absence of PhTx within each genotype. Absolute values for mEPP, EPP and quantal content are presented in supplemental figures.

We assessed PHP in three previously described, strong hypomorphic ($mys^{b8}$, $mys^{42}$) and null ($mys^{1}$) mutations that disrupt the *mys* gene (Beumer et al., 1999; Bunch et al., 1992). PHP is completely blocked in all three allelic combinations (Figure 3B, C, blue). There is a significant decrease in baseline EPP amplitude only in the strongest *mys* allelic combination ($mys^{1/42}$), primarily due to a decrease in mEPP amplitude without a compensatory change in presynaptic release (Supplemental Figure 2A). The observation that quantal content does not change despite the observed decrease in mEPP amplitude in the $mys^{1/42}$ mutant is consistent with *mys* being necessary for PHP.

Next, we demonstrate that motoneuron-specific expression of *mys-RNAi* (*OK371-Gal4*) blocks expression of PHP compared to *Gal4* control (Figure 3D; Supplemental Figure 3A), including experiments at physiological calcium (Figure 3F, G; note there is no significant effect on baseline EPSC prior to PhTx; p=0.31, Student's t-test, two tailed). By contrast, PHP is still significantly expressed following muscle-specific expression of *mys*-RNAi (Figure 3E; *BG57-Gal4;* Supplemental Figure 3C). In agreement, presynaptic expression of a *UAS-Mys* transgene significantly rescues PHP the $mys^{1/42}$ background, although not precisely to control values (*OK371-Gal4;* Figure 3D, MN rescue; Supplemental Figure 3A), while postsynaptic expression of *UAS-mys* failed to achieve significant rescue of PHP (Figure 3D; Supplemental Figure 3A). Thus, although we cannot completely rule out some postsynaptic participation, *mys* is essential presynaptically.

Integrins have been demonstrated to influence the growth of the *Drosophila* NMJ, acting predominantly within the postsynaptic muscle cell (Beumer et al., 1999; Broadie et al., 2011). Here, we show that the $mys^{1/42}$ mutant NMJ has a small decrease in bouton number, consistent with prior observations (Beumer et al., 1999). However, there is no significant difference in active zone number (Supplemental Figure 4) as determined by the number of anti-Bruchpilot puncta (BRP; Wagh et al., 2006). Since active zone number remains constant, it seems very unlikely that a minor change in bouton numbers could account for the deficit in PHP, consistent with prior data (Orr et al., 2017).

Next, we tested a required function for alpha-Integrin. It was previously established the alpha-Integrin encoded by *multiple edematous wings* (*mew*) is expressed and localizes to the larval NMJ (Broadie et al., 2011). Here, we demonstrate that presynaptic RNAi-mediated knockdown of *mew* completely blocks expression of PHP (Figure 3H, I). We observe a small, but significant, decrease in baseline EPSP amplitude compared to *Gal4* controls, but only a trend ($p>0.05$) toward a decrease in baseline presynaptic release (quantal content; Supplemental Figure 2B).

To further probe the necessity of an alpha/beta-Integrin interaction during PHP, we took advantage of two point mutations previously demonstrated to diminish the association of alpha- and beta-Integrin, consistent with suppression of integrin activation. The *D807R* mutation reverses a critical charge in a highly conserved HDRK motif, thereby disrupting the ‘closed’ inactive conformation of alpha and beta-Integrin (Figure 3J). The *G792N* mutation resides within the beta-Integrin transmembrane domain, forcing a protein conformation that favors dissociation of the alpha- and beta-Integrins (Li et al., 2003; Pines et al., 2011). We recorded from transgenic animals that constitutively express either the *D807R* or *G792N* mutation ($Ubi{:}mys^{D807R}$-*YFP* and $Ubi{:}mys^{G792N}$-*YFP*) and demonstrate that they completely block expression of PHP (Figure 3K, L). We note that the $Ubi{:}mys^{D807R}$-*YFP* mutant dominantly impairs baseline EPSP amplitude (Figure 3K; $p=0.31$, ANOVA with Tukey correction for multiple comparisons). This is consistent with prior evidence in *Drosophila* demonstrating that the $Ubi{:}mys^{D807R}$-*YFP* mutant, but not the $Ubi{:}mys^{G792N}$-*YFP* mutation, affects cytoplasmic adaptor protein recruitment by Mys (Pines et al., 2011). Both transgenes localize to the NMJ and protein levels are approximately twice that observed in animals with endogenously tagged Mys protein (Supplemental Figure 5F–I). We note that EPSP amplitudes are diminished only in $Ubi{:}mys^{D807R}$-*YFP* (Figure 3K) and this effect is, therefore, unlikely to account for the commonly observed block in PHP (Figure 3L). Together, these data underscore a required function for alpha/beta-Integrin association in the mechanism of PHP.

Next, we deployed an additional *mys* point mutation. The *S196F* mutation resides in the beta-Integrin head domain and allows adhesive ECM interactions, but prevents conformational changes that transduce extracellular signaling to the cell interior (Figure 3J; Pines et al., 2011). We generated CRISPR knock-in animals harboring the $mys^{S196F}$ mutation and demonstrate that the $mys^{S196F}$-*GFP* protein localizes to the NMJ (Supplemental Figure 5E). These knock-in animals are homozygous lethal, consistent with this being a severe loss-of-function mutation. Therefore, we assessed PHP in heterozygous $mys^{S196F}$ mutants. Remarkably, we find that PHP is completely blocked, on average (Figure 3 J–L). These data underscore the importance of signal transduction for the expression of PHP.

As a final control we quantified synaptic bouton number and active zone numbers. Although bouton numbers are diminished in both the $Ubi{:}mys^{G792N}$-*YFP* and heterozygous $mys^{S196S}$ mutations, only the heterozygous $mys^{S196S}$ mutant shows a significant decrease in active zone number (Supplemental Figure 4). Since all five loss of function alleles block PHP, there no correlation between altered synapse growth and PHP expression, consistent with previously published literature demonstrating molecular dissociation between expression of PHP and synaptic growth control (Goold & Davis, 2007; Orr et al., 2017).

### Homeostatic potentiation of the readily releasable vesicle pool requires beta-Integrin.

Estimates of baseline RRP are statistically similar comparing wild type and the *mys*$^{1/42}$ mutant, and application of PhTx causes a similar decrease in mEPSC amplitude in wild type and the *mys*$^{1/42}$ mutant. However, while wild type responds to PhTx with an increase in the RRP, thereby maintaining cumulative EPSC amplitude, the *mys*$^{1/42}$ mutant RRP remains unchanged following PhTx application resulting in a significant drop of the cumulative EPSC amplitude.

It is also apparent that the *mys*$^{1/42}$ mutation alters the short-term dynamics of synaptic vesicle release (Figure 4C). Therefore, we explored the origin of this phenotype. We find no change in active zone appearance or active zone length in the *mys*$^{1/42}$ mutant compared to wild type (Figure 4G, H). However, when we quantified synaptic vesicle number and distribution we identified two phenotypes: 1) a significant decrease in vesicle number in *mys*$^{1/42}$ (Figure 4H) and 2) a selective loss of docked vesicles that reside at a distance from the active zone center where calcium channels reside (Figure 4I). Consistent with these observations, we demonstrate that the *mys*$^{1/42}$ mutant is insensitive to the slow calcium buffer (EGTA-AM). The EGTA-sensitive synaptic vesicle pool is related to vesicles that are loosely-coupled to calcium channel influx, consistent with vesicles that reside at a greater physical distance from sites of calcium entry (Figure 4D–F) (Genç & Davis, 2019; Müller et al., 2015; Schneggenburger & Neher, 2005). We note that several recent publications provided evidence that regulation of the docked vesicle pool is an essential mechanism underlying PHP at the *Drosophila* NMJ (Harris et al., 2018; Müller et al., 2015; Weyhersmüller et al., 2011).

Finally, we returned to perform a similar analysis at the NMJ of wild type and *ITGB1 cKO* mice. As previously documented at the mouse NMJ (Miteva et al., 2020), application of EGTA-AM had no effect on wild type EJC amplitude or short-term plasticity (Supplemental Figure 1E–G). We find that the same is true for the *ITGB1 cKO* (Supplemental Figure 1E–G). However, EGTA-AM does cause EPSC broadening and delayed time to peak amplitude, without altering the underlying mEPSCs (Supplemental Figure 1H–K). Interestingly, EPSCs recorded from ITGB1 cKOs are significantly broader than wild type at baseline and have a slower time to peak, and these parameters are not further altered following application of EGTA-AM (Supplemental Figure 1H–K). This suggests that vesicles are differentially coupled to sites of calcium influx in the *ITGB1 cKO*. Thus, although the NMJ of mouse and *Drosophila* are clearly distinct, loss of integrin signaling seems to impair vesicle coupling to sites of presynaptic calcium influx in both systems.

### Beta-Integrin functions as a PlexinB co-receptor.

At the *Drosophila* NMJ, trans-synaptic signaling during PHP is mediated by a secreted Semaphorin (Sema2b), which binds presynaptic PlexinB (PlexB) receptors (Orr et al., 2017). Here, we confirm a presynaptic requirement for PlexB by presynaptic over-expression of a PlexB transgene that is unable to bind Sema2b (Guajardo et al., 2019). PHP is blocked (Supplemental Figure 6F–I). It was recently demonstrated that Mys functions as a PlexB co-receptor during dendrite development in *Drosophila* peripheral sensory neurons (Meltzer et al., 2016). Thus, we hypothesized that Mys could serve a similar function during PHP.

We employed a proximity ligation assay using epitope-tagged *UAS-Flag-Mys* and *UAS-myc-PlexB* transgenes (Meltzer et al., 2016), co-expressed specifically in presynaptic motoneurons (*OK371-Gal4*). We note that presynaptic Flag-Mys protein is present at levels that are similar to an endogenously tagged *Mys* gene (Supplemental Figure 5B). Presynaptic myc-PlexB protein is also expressed at levels that are similar to an endogenously tagged *PlexB* gene (Supplemental Figure 6A–E). We observe a robust interaction between Mys and PlexB compared to controls (Figure 5A). Reaction product was clearly visible at the NMJ and in the peripheral axons leading to the NMJ. Next, we confirmed the Mys-PlexB association biochemically with a pull-down experiment using the same transgenes expressed in motoneurons (Figure 5C). Remarkably, when this pull-down assay was repeated in the background of a *sema2b* null mutation, the association of Mys and PlexB was abolished (Figure 5C). This result confirms the specificity of the Mys-PlexB interaction, and indicates that it is ligand-dependent. We hypothesize that Sema2b either stabilizes the Mys-PlexinB co-receptor complex, or that Sema2b-dependent conformational changes in the PlexinB protein are required for the biochemical association of PlexinB with Mys. We note that the PlexinB-Mys interaction was previously mapped to an extracellular, membrane proximal region of PlexinB (Meltzer et al., 2016).

Given that PlexB and Mys physically interact, we asked whether these genes also genetically interact during PHP. We analyzed double *heterozygous* mutant animals (Frank et al., 2009; Genç et al., 2020; Ortega et al., 2018). We demonstrate that PHP is completely blocked in double heterozygous animals (Figure 5D; Supplemental Figure 5A). We note that the heterozygous *mys*$^{1}$*/+* mutant alone causes a significant 50% suppression of PHP. However, since PHP is fully expressed in *PlexB/+* mutant, the complete block of PHP in the double heterozygous combination cannot be attributed to an additive effect of the two heterozygous mutations. We conclude that PlexB and Mys interact both physically and genetically for expression of PHP.

Finally, we tested whether the induction of PHP involves enhanced Sema2b-PlexB-Mys signaling (see also Orr et al., 2017). To do so, our proximity ligation assay was performed on NMJ that had been pre-treated in either PhTx or control saline for 1hr. We observe a significant, PHP-dependent increase in proximity-ligation reaction product (puncta) number/NMJ, as well as a PHP-dependent increase in the average size of individual reaction puncta (Figure 5B). Thus, not only do PlexB and Mys proteins interact in a Sema2b dependent manner, but the PlexB-Mys interaction is also potentiated following the rapid induction of PHP.

## Talin localizes to the presynaptic active zone and is necessary for PHP

*Talin* encodes a multi-domain, cytoplasmic scaffolding protein that transitions from an inactive cytoplasmic protein dimer to an activated monomer that interacts with phospholipids in the plasma membrane and binds the cytoplasmic tail of beta-Integrin (Klapholz & Brown, 2017). Talin participates in the oligomerization of activated integrins, thereby facilitating the creation of signaling domains and focal adhesions (Klapholz & Brown, 2017). Talin also binds actin, promoting the formation of actin filaments upon integrin activation (Michael & Parsons, 2020). The action of Talin within the presynaptic terminal remains virtually unknown (Morgan et al., 2004).

A highly conserved Talin ortholog exists in *Drosophila* (Figure 6A). We inserted a BFP coding exon into the endogenous *Talin* locus (Figure 6A). Talin-BFP is broadly distributed at the NMJ, both pre- and postsynaptically (Figure 6A). When analyzed using super-resolution, structured illumination microscopy (SIM), assessing single confocal sections, we find elongated Talin micro-domains within the volume of the presynaptic nerve terminal (Figure 6A, single plane). Surprisingly, a portion of presynaptic Talin-BFP foci were observed to co-localize with the active zone marker Bruchpilot (Brp), residing at the cytoplasmic face of the presynaptic active zone (Figure 6B). We used machine-learning algorithms to identify all Talin-BFP foci that co-localize with presynaptic Brp, revealing that 60% of Brp puncta are associated (within 120 nm) with Talin-BFP (Figure 6B).

Given our evidence of rapid integrin activation following PHP induction in both mouse and fly, we asked whether Brp-associated Talin puncta increase in size or number following induction of PHP. By identifying all Brp-associated Talin puncta, we demonstrate that pre-incubation in PhTx induces a 250% increase in the average size of Talin puncta, without altering the number of Brp puncta that harbor Talin puncta (N>10 animals; n>1000 active zones). Finally, we repeated this analysis in a *sema2b* null mutant background and show that the increase in Brp-associated Talin puncta volume is abolished (Figure 6B). Importantly, the number of Brp-associated Talin puncta at baseline remain unchanged in the *sema2b* mutant.

To determine whether presynaptic Talin is necessary for PHP, we depleted presynaptic Talin using *UAS-Talin-RNAi* (*OK371-Gal4*). We find that PHP is completely blocked (Figure 6D; Supplemental Figure 7C). Because *Talin* deletion is lethal, we sought independent methods to selectively and specifically interfere with the Talin-Mys protein-protein interaction. In mammals, mutations have been identified that disrupt Talin binding to ITGB1, one residing in the ITGB1 cytoplasmic domain and three others residing in Talin (Ellis et al., 2011; Pines et al., 2011). We acquired transgenic lines that ubiquitously express synonymous mutations in *Drosophila mys* and *Talin* (*Ubi:mys*$^{L796R}$*-YFP* and *Ubi:Talin*$^{IBS}$*-GFP*) (Pines et al., 2011). First, we confirmed that Mys$^{L796R}$ protein has diminished Talin binding, but still localizes to the NMJ (Figure 6E). Then, we show that Mys$^{L796R}$ protein overexpression completely blocks expression of PHP (Figure 6F; Supplemental Figure 7A, B). Next, we repeated these experiments for the *Ubi:Talin*$^{IBS}$*-GFP* mutant (Figure 7). We confirmed that the *Ubi:Talin*$^{IBS}$*-GFP* mutant impairs the ability of Mys/Mew protein complexes to pull down Talin (Figure 7B). Then, we demonstrate that overexpression of *Ubi:Talin*$^{IBS}$*-GFP* blocks PHP, assayed by measuring the PHP-dependent expansion of RRP (Figure 7C, D). We note that baseline effects on initial EPSC amplitude and altered release dynamics are nearly identical to those observed in the *mys* mutant (compare Figure 7C, E with Figure 4A, C, E). Again, as a control, we find that *Ubi:Talin*$^{IBS}$*-GFP* expressed protein localizes to the NMJ and is not highly overexpressed (Supplemental Figure 7F–H).

Finally, we pursued genetic interactions between the *Talin* mutant and both the *mys* and *PlexB* gene mutations. Heterozygous *Talin* mutants have normal baseline synaptic transmission and show robust PHP. However, when tested as a double heterozygous combination with a *mys* heterozygous mutant or a *PlexB* heterozygous mutant, we observe a selective block of PHP without significant effects on baseline neurotransmitter release (Supplemental Figure 5C, D). Taken together, we define *Drosophila* Talin as a presynaptic, active zone localized protein and demonstrate that Talin-Mys binding is essential for the induction and/or expression of PHP.

## Presynaptic Focal Adhesion Kinase (FAK) is essential for PHP.

The *FAK* gene encodes a highly conserved serine threonine kinase that facilitates integrin activation and also functions as a downstream mediator of integrin signaling with diverse cytoplasmic signaling targets (Schlaepfer et al., 1999; Webb et al., 2004). We tested a transposon insertion mutation that resides in the *FAK* locus ($FAK^{KG304}$), predicted to be a loss-of-function allele, and one that survives to late larval stages (Grabbe et al., 2004; Tsai et al., 2008). We also assessed the effects of two independent *UAS-FAK-RNAi* lines, driven in presynaptic motoneurons by *OK371-Gal4*. We demonstrate that all three *FAK* perturbations completely block the expression of PHP (Figure 6G; Supplemental Figure 7E).

## Pre-assembled beta-Integrin/PlexB signaling complexes drive homeostatic overshoot

To further examine how integrin-mediated signaling instructs PHP, we took advantage of a mutation causing constitutively active ITGB1 signaling (Luo et al., 2009; Pines et al., 2011). We analyzed the orthologous activating mutation in *Drosophila Mys* (L211I) using animals that constitutively express this variant ($Ubi{:}mys^{L211I}$-*YFP*). The $Ubi{:}mys^{L211I}$-*YFP* expressed protein localizes to the NMJ (Supplemental Figure 5F–I) without altering baseline synaptic transmission (Figure 8A, B; Supplemental Figure 8A). However, following application of PhTx to $Ubi{:}mys^{L211I}$-*YFP* animals, quantal content is potentiated significantly beyond that observed at baseline and in controls, indicative of PHP overshoot (Figure 8A–C; Supplemental Figure 8A, C). To further assess PHP overshoot, we plot mEPSP amplitude versus quantal content for each individual recording (Figure 8D). A significant negative correlation exists in controls (Figure 8D). This negative correlation persists in the $Ubi{:}mys^{L211I}$-*YFP* animals, but the relationship is significantly steeper (Figure 8D).

We next asked whether the $Ubi{:}mys^{L211I}$-*YFP* mutant is sufficient to bypass a requirement for extracellular ligands that are thought to be essential for PHP. Two extracellular ligands are required for expression of PHP: 1) Sema2b (see above) and 2) Endostatin, which is a matrix-derived signaling protein released upon proteolytic cleavage of the *Drosophila* Collagen18 ortholog Multiplexin (Wang et al., 2020; Wang et al., 2014). First, we provide evidence that Endostatin also binds the Mys protein (Supplemental Figure 8B). Next, we demonstrate that PHP is fully expressed in the $Ubi{:}mys^{L211I}$-*YFP*; *multiplexin* double mutant (Figure 8B, C; Supplemental Figure 8A). Then, we generated animals expressing $Ubi{:}mys^{L211I}$-*YFP* in the background of postsynaptic *Sema2b* knockdown, a condition that is sufficient to block PHP (Orr et al., 2017). In these animals, PHP remains blocked (Figure 8B, C; Supplemental Figure 8A). These data argue that Endostatin functions upstream of integrin activation, possibly serving to initiate integrin activation (Park & Goda, 2016; Ross et al., 2017; Wang et al., 2018). Sema2b, however, seems to function in concert with activated integrin, consistent with biochemical evidence that *Sema2b* is necessary for the integrity of the Mys-PlexinB co-receptor signaling complex (Figure 5C).

Intriguingly, we subsequently discovered that the Mys$^{L211I}$ mutant protein pulls down dramatically more PlexB compared to controls (Figure 8E). To further probe this effect, we repeated our proximity ligation assay for the Mys-PlexinB interaction *in situ,* doing so in the presence of *Ubi:mys*$^{L211I}$*-YFP* gene expression. We find a highly significant (>2-fold) increase in reaction product puncta area in the mutant compared to controls (*Ubi:mys-YFP*) (Figure 8F). Finally, we quantified the size of *Ubi:mys-YFP* puncta that co-localize with the presynaptic membrane marker anti-HRP (see Figure 3A, white arrows). We find an approximate 5-fold increase in presynaptic Mys-YFP puncta size in the *Ubi:mys*$^{L211I}$*-YFP* mutant compared to control (*Ubi:mys-YFP*). We then repeated this assay in the presence or absence of PhTx pre-incubation. PhTx dramatically increases synaptic puncta size in controls, reaching a level observed in the *mys*$^{L211I}$ mutant (Figure 8F). However, when we applied PhTx to the *Ubi:mys*$^{L211I}$*-YFP* mutant, no additional change in puncta size was observed (Figure 8F). Based on evidence from three independent visual and biochemical assays, we conclude that the Mys$^{L211I}$-YFP generates pre-configured, pre-expanded, Mys-PlexB co-receptor complexes, reaching a maximal size that cannot be further expanded following application of PhTx and initiation of PHP. However, since baseline transmission remains unaltered in the *Ubi:mys*$^{L211I}$*-YFP* mutant, these pre-configured complexes appear to be poised for PHP expression, but lack an essential molecular component or molecular trigger.

If the *Ubi:mys*$^{L211I}$*-YFP* mutant induces pre-assembled signaling complexes, we reasoned that the *rate* of PHP expression should be increased following acute application of PhTx. In wild type, application of PhTx causes a rapid decrease in mEPSP amplitude (<1min) followed by a significant potentiation of quantal content over a period of ~3 minutes (Figure 8G, H), consistent with a previously published time course (Frank et al., 2006). By contrast, in the *Ubi:mys*$^{L211I}$*-YFP* mutant, we observe an immediate, statistically significant increase in quantal content, evident in less than 1 minute (Figure 8H, Supplemental Figure 8C). The potentiation of quantal content in the *Ubi:mys*$^{L211I}$*-YFP* mutant is significantly more rapid and of greater magnitude than that observed in wild type (Figure 8I). However, EPSP amplitudes do not over-shoot baseline (Figure 8A, D). It should be noted that the magnitude of PHP is routinely diminished when PhTx is applied to muscle cells that have been previously impaled by a sharp recording electrode (Frank et al., 2006). None-the-less, these data clearly demonstrate that PHP is accelerated and exceeds wild type levels in the *Ubi:mys*$^{L211I}$*-YFP* mutant.

## DISCUSSION

We provide insight into the presynaptic signaling systems that initiate, promote and amplify the homeostatic potentiation of synaptic vesicle release (PHP). Based upon these data, we propose a sequence of events that drive PHP. First, we provide evidence that homeostatic signaling is initiated by Endostatin-dependent activation of presynaptic alpha- and beta-Integrin. Both alpha- and beta-Integrin are necessary for PHP, as is their initial biochemical association. Furthermore, we demonstrate that Endostatin binds beta-Integrin and functions upstream of beta-Integrin activation during PHP. Thus, we propose that PHP is initiated by the proteolytic release of Endostatin from the synaptic extracellular matrix, an advance beyond prior publications that established the necessity of Endostatin (Wang et al., 2014).

Second, we provide evidence that PHP progresses through the formation of a presynaptic signaling complex involving an interaction of activated beta-Integrin with Semaphorin2b-bound PlexinB. Since genetic activation of beta-Integrin cannot bypass a Semaphorin2b null mutation, and the association of these co-receptors is dependent on Semaphorin2b, we conclude that Semaphorin2b drives the progression of PHP.

Third, we provide evidence that the amplification of PHP, expressed as a progressive increase in presynaptic quantal content over time, is achieved by a physical expansion of activated Semaphorin2b/beta-Integrin/PlexinB signaling complexes that seem to reside at or adjacent to the presynaptic active zone. Complex expansion was documented by proximity ligation, direct imaging of beta-Integrin in mouse and *Drosophila,* biochemical association of beta-Integrin with PlexinB and quantitative Talin imaging at the presynaptic active zone. Importantly, a beta-Integrin activating mutation (L211I) led to pre-expansion of signaling foci and accelerated both the rate and extent of PHP, thereby directly linking foci expansion to the regulation of PHP.

The identification of a signaling complex that expands (and presumably contracts) to control the expression of PHP is quite unique when considering the existing literature on mechanisms of synaptic plasticity at mature synapses. However, as a mechanism of signaling, this process is quite prevalent in other areas of biology, particularly the immune system (Houtman et al., 2005). Mechanistically, we note that expansion of these homeostatic signaling complexes is entirely consistent with the well-documented dynamics of integrin-based focal adhesions at the leading edge of migrating cells (Huttenlocher & Horwitz, 2011) and the oligomerization of Plexin receptors when activated by secreted Semaphorin dimers (Janssen et al., 2012; Pascoe et al., 2015). Indeed, the temporal dynamics of focal adhesion assembly in migrating cells is well matched to the time-course of PHP induction, measured electrophysiologically (Berginski et al., 2011).

## Model: Vesicle Capture and Release.

It is well established that Talin promotes the formation of actin filaments, thereby coupling the ECM to the sub-membranous actin cytoskeleton in migrating cells (Klapholz & Brown, 2017). By contrast, PlexinB signals via the flavoprotein monooxygenase MICAL to modulate G-actin, favoring destabilization of actin filaments, a process that is necessary for PHP (Orr et al., 2017; Terman et al., 2002; Wu et al., 2018). Thus, simultaneous activation of beta-Integrin and PlexinB within a single signaling complex, at or adjacent to sites of vesicle fusion, should initiate opposing activities directed to the synaptic actin cytoskeleton (Figure 8).

We propose a model to conceptualize the opposing actions of Talin and MICAL during PHP. Recent evidence supports the existence of two pools of presynaptic actin. One pool of actin resides within the synaptic vesicle field that surrounds each active zone. This pool has been variously implicated in vesicle tethering, vesicle movement and as a substrate for the mechanisms of synaptic plasticity (Chenouard et al., 2020; Maschi et al., 2018; Sankaranarayanan et al., 2003). A second pool of actin resides close to the plasma membrane (cortical actin) and influences vesicle fusion (Bleckert et al., 2012; Eitzen, 2003; Morales et al., 2000; Papadopulos et al., 2013; Wang & Richards, 2011). In particular, at the lamprey giant synapse, selective pharmacological stabilization of the cortical actin pool blocks all spontaneous and evoked vesicle fusion (Bleckert et al., 2012). We speculate that Talin and MICAL may differentially act upon these separate pools of synaptic actin. Talin is positioned to promote formation of filamentous actin within the synaptic vesicle pool, possibly promoting vesicle recruitment to the active zone. MICAL, by contrast, is coupled to PlexinB near the plasma membrane where it could destabilize cortical actin and facilitate vesicle release. Thus, when activated in parallel, Talin and MICAL suggest a mechanism of synaptic vesicle 'catch and release' that could reasonably potentiate the RRP during PHP (Figure 8). We acknowledge that our model is reductionist, adhering to signaling components that are currently known to influence PHP, ignoring other potential signaling mechanisms that could be initiated by co-activation of beta-Integrin and PlexinB. Clearly, there is potential for additional signaling complexity and regulation.

# STAR METHODS

## RESOURCE AVAILABILITY

**Lead Contact—**Further information and requests for resources and reagents should be directed to and will be fulfilled by the Lead Contact, Graeme W. Davis (Graeme.Davis@ucsf.edu).

### Materials Availability

- No unique plasmids suitable for deposition have been generated in this study.
- No unique mouse lines have been generated in this study.
- All materials generated in this manuscript will be distributed in a timely manner upon request including *Drosophila* stocks that are not commonly available in public data bases.

### Data and Code Availability

- All primary data reported in this paper will be shared by the lead contact upon request.
- This paper does not report original code.
- Any additional information required to reanalyze the data reported in this paper is available from the lead contact upon request.

## EXPERIMENTAL MODEL AND SUBJECT DETAILS

**Fly stocks and genetics—**All *Drosophila melanogaster* stocks were grown at 22–25°C on normal food. Male and female animals were used during experimental procedures. For experiments testing the effects of *mys* point mutations tagged with a fluorescent protein, we used animals with a fluorescently tagged wildtype *mys* as control animals. All *mys* mutants animals were maintained as heterozygous stocks due to the lethality of *mys* LOF alleles. Animals with the *mys*$^{b42}$ mutation were raised at 25°C for experiments. All experiments were performed in the third instar larva. Refer to key resource table for each *Drosophila* line used and its origin.

**Mouse Knockout and genetics—**The presynaptic conditional knockout (cKO) of Itgb1 in motor neurons was achieved by crossing two stock lines: *HB9*$^{+/+}$*;Itgb1*$^{loxP/loxP}$ *and HB9*$^{Cre/+}$*;Itgb1*$^{loxP/+}$. These two lines were maintained as separate colonies and bread to produce homozygous cKO and homozygous loxP sibling controls. These lines are both in the B6;129 Background. All data comparisons were made using male and female age matched *loxP/loxP* and cKO/cKO litter mates. Electrophysiology Data were collected from p90 staged mice. Mice were genotyped using Transnetyx genotyping services. Mouse genotypes from ear biopsies were determined using real time PCR with specific probes designed for each gene (Transnetyx, Cordova, TN). Probe sequences are the intellectual property of Transnetyx.

All data was collected in accordance and to the standards with the Institutional Animal Care Use Committee (IACUC) at UCSF. Our Animal protocol for this study was approved by IACUC (AN173616-01A through 03/19/2018 and currently AN108729-01). Protocols conform to IACUC approved regulatory standards.

**CRISPR generation *Drosophila* tagged proteins—**The following stocks were generated for this study: *mys*$^{GFP}$, *mys*$^{S196F\ GFP}$ and *talin*$^{BFPMyc}$. *Mys* stocks were generated using CRISPR endogenous gene replacement strategy. Endogenous gene replacements were generated using a scarless CRISPR strategy (http://flycrispr.molbio.wisc.edu/scarless). Donor and gRNA plasmids were co-injected into vas-Cas9 expressing *Drosophila* embryos (either BDRC 56552 or 51324 stocks). The donor plasmid contained the gene of interest, ~1 kb of homologous sequence upstream and downstream of the genomic insertion sites, and a dsRed cassette was the selection marker. Additionally, the PAM sites in the donor plasmid were mutated. These homologous sites in the genome were used to guide the initial Cas9 mediated cleavage of the endogenous genomic locus of interest. This prevents the cleavage of the transgene after homology directed repair (HDR) insertion. The gRNA plasmid contained two gRNA sequences to direct Cas9 cleavage of sites upstream and downstream of the target genomic region to be replaced. *Talin*$^{BFPMyc}$ was generated phiC31-mediated RMCE using the strategy described in Nagarkar-Jaiswal et al. 2015. Bestgene is the injection service used to generate transgenic flies. Transgenic animals were verified by PCR and sequencing. The dsRed selection marker cassette was removed by crossing flies to 3xP3 transposase expressing flies. Through fluorescence screening (GFP+ dsRed−), we selected the progeny of this cross to found the final *Drosophila* lines. Transgenic animals were verified by PCR and sequencing a second time.

## METHOD DETAILS

All experiments conducted in this study were performed on both sexes. We performed power analyses to determine the sample sizes for each experiment. No data collected was excluded from our analysis and scientists were not blinded from genotype. When assessing the electrophysiology of the *Drosophila* or mouse NMJ, at least 3 animals were used for each condition and genotype. Multiple muscle fibers were recorded from each animal. Each fiber is counted as one n.

***Drosophila* electrophysiology from the neuromuscular junction (NMJ)—**Sharp-electrode recordings were made from muscle 6 in abdominal segments 2 and 3 from third-instar larvae using an Axoclamp 900A amplifier (Molecular Devices), as described previously (Frank et al. 2006, Muller et al. 2012). Recordings were made in HL3 saline containing the following components: NaCl (70 mM), KCl (5 mM), $MgCl_2$ (10 mM), $NaHCO_3$(10 mM), sucrose (115 mM), trehalose (5 mM), HEPES (5 mM), and $CaCl_2$ (as indicated in figures). For acute pharmacological homeostatic challenge, unstretched larva were incubated in Philanthotoxin-433 (PhTX; 15 μM; Sigma-Aldrich) for 10 min. (Frank et al. 2006). Recordings were excluded if the resting membrane potential (RMP) was more depolarized than −55mV. A threshold 40% decrease in mEPSP amplitude, below average baseline, was used to confirm the activity of PhTX. Miniature spontaneous events were analyzed using MiniAnalysis 6.0.0.7 (Synaptosoft), averaging at least 100 individual mEPSP (or mEPSC) events. EPSP (or EPSC) amplitudes were analyzed in IGOR Pro (Wave-Metrics) with previously routines (Müller et al., 2015). Quantal content was calculated by dividing mean EPSP (or EPSC) by mean mEPSP (or mEPSP). Estimates of RRP were achieved by quantifying cumulative EPSC amplitudes during prolonged high-frequency stimulation and normalization to the amplitude of the underlying spontaneous mEPSC amplitude, as previously performed (Müller et al., 2012, 2015; Weyhersmüller et al., 2011; Wang et al., 2016). Best-fit curves for mEPSP amplitude versus quantal content were fit in Prism 9 (GraphPad) using a power function for all wild-type data points +/−PhTX. 95% data intervals were fit in IGOR Pro (Wave-Metrics) using a power function. Each recording paradigm (i.e. genetic mutant an or treatment) was biologically replicated at least 3 times. Muscle membrane potentials were held at −65 mV during two-electrode voltage clamp experiments.

**Mouse electrophysiological recording from the neuromuscular junction—**Mice (p90), of both sexes, were administered Isoflurane and euthanized by cervical dislocation. Hemidiaphragms were recovered from the thoracic cavity, with the phrenic nerve intact. Hemi diaphragm preparations were placed in a recording chamber and stained with M 4-(4-diethylaminostyryl)-N-methylpyridinium iodide (Invitrogen) to visualize the NMJs. The preparations were perfused at a speed of 3–6 ml/min with an external solution containing the following (in mM): 118 NaCl, 0.7 $Mg_2SO_4$, 2 $CaCl_2$, 3.5 KCl, 26.2 $NaHCO_3$, 1.7 $NaH_2PO_4$, and 5.5 glucose, pH 7.3–7.4 (at 20–22°C), equilibrated with 95% $O_2$ and 5%$CO_2$. Contraction of the diaphragm was prevented by the application of 1–3mM conotoxin GIIIB (Peptide Institute, Inc.), which inhibits muscle specific voltage sensitive sodium channels. mEPP and EPP intracellular recordings were obtained using single electrode current clamp. mEPSC and EPSC intracellular recordings were obtained using two-electrode voltage clamp. Muscle fibers voltage was held at −65 mV during mEPSC and EPSC acquisition. 10 action potential evoked responses were recorded and averaged for each NMJ and we obtained 30 mEPP (or mEPSC) recordings or 2-minute period, for analysis. We recorded from multiple endplates from a single hemidiaphragm and counted each endplate as single data point. Each experimental condition was recorded from ≥ 3 mice. Therefore, each experimental or control condition was collected from ≥ 3 biological replicates, unless otherwise indicated. No collected data was excluded from this study. D-Tubocurarine was perfused onto the preparation to pharmacologically induce PHP at the mouse NMJ, with a final concentration of 0.1 μM (Wang et al., 2016). EGTA-AM, a calcium chelator, that has slow calcium-binding kinetics perfused onto the preparation with a final concentration of 50 μM. Estimates of RRP were achieved by quantifying cumulative EPSC amplitudes during prolonged high-frequency stimulation and normalization to the amplitude of the underlying spontaneous mEPSC amplitude, as previously performed (Müller et al., 2012, 2015; Weyhersmüller et al., 2011; Wang et al., 2016). To acutely disrupt Itgb1 for electrophysiological recording, function blocking antibodies or RGD peptides were applied to the saline profusion either before or after PHP was induced by D-Tubocurarine application, depending on the experimental design. Antibodies and RGD Peptides were applied for 1 hour before recording to ensure complete ITGB1 inhibition. The final profusion concentrations for each inhibitor treatment are as follows: mAb AIIB2 (25 μg/mL), mAb 9EG7 (160 μg/mL), and RGD peptide (100 μg/mL).

***Drosophila* immunohistochemistry—**Standard immunohistochemistry was performed as previously described (Pielage et al., 2005). In brief, filleted third instar larvae were fixed in either Bouin's fixative (Sigma-Aldrich, 5 minutes) or 4% PFA (Affymetrix, 30 minutes), as indicated for each antibody below. Preps were washed in PBT (PBS with 0.1% Triton) for 1 hour, then incubated overnight at 4° in primary antibody in PBT. Larval fillets stained for the following primary antibodies were fixed with Bouin's: mouse anti-BRP (1:100, Developmental Studies Hybridoma Bank), rabbit anti-Discs large (Dlg, 1:1,000, Budnik et al., 1996), mouse anti-Integrin beta PS (Myospheroid, CF.6G11, 1:10), mouse anti-GFP 3E6 (1:500, Life Technologies), rabbit Anti-c-Myc (1:1000, Sigma-Aldrich) and mouse anti-FLAG M2 (1:1000, Sigma-Aldrich). Preps were washed in PBT for 1 hour and incubated in secondary antibody in PBT for 1 hour at room temperature. Alexa-conjugated secondary antibodies were used at 1:500 and FITC-, Cy3-and Cy5-conjugated HRP was used at 1:100 (Jackson Immuno-research Laboratories). Preps were mounted in Vectashield (Vector). The presynaptic motor neuron terminals (labeled with anti-HRP) defined ROI for quantifying synaptic protein abundance at the NMJ, such as quantifying $mys^{EYFP}$ and $mys^{L211I.EYFP}$ puncta, ± PhTx. PLA Assays was performed with Duolink® In Situ Red Starter Kit Mouse/Rabbit. The kit protocol was followed. The *Gal4*/UAS system was used to express *mys* and *PlexB* transgenes in motor neurons (*UAS-FLAG-mys* and *UAS-Myc-PlexB* with *OK371-Gal4*). Larva were fixed in 4% PFA for 20min, blocked for 1 hour, and incubated with mouse anti-FLAG (1:500) and rabbit anti-Myc (1:1000). See key resource table for antibody specifics. For experiments using the *mys* GOF activating mutation, $mys^{EYFP}$ or $mys^{L211I.EYFP}$ were crossed to animals expressing UAS-Myc-PlexB in motor neurons (*OK371- Gal4*). In this case, mouse anti-GFP (1:500) and rabbit anti-Myc (1:1000) antibodies were used. In some experiments, PhTx (15 μM) was applied for 1 hour to intact larval preparations before fixation. We used the presynaptic motor neuron axons and terminals (anti-HRP) to define ROI when quantifying PLA puncta at the NMJ, ± PhTx.

**Mouse Immunohistochemistry—**Hemidiaphragms were collected as described above. Next, tissue was fixed in 2% PFA for 15 mins or overnight at 4° C for NMJ morphological analysis. Diaphragms were then washed in 2% PBST for 1 hour to permeabilizes the tissue for antibody penetration. Then we blocked the tissue with 4% normal Goat serum for 1 hour in PBST. Diaphragms were incubated over night at 4 degrees Celsius in primary antibodies, washed with 0.1% PBST for 2 hours at room temperature, and incubated at room temperature for 4 hours in secondary antibodies. A final wash was performed in 0.1% PBST for 2 hours. The following primary antibodies were used on mouse tissue: mouse anti-Bassoon monoclonal (1:100), anti-Neurofilament-H (1:1000), mouse anti-ITGb1 9EG7 (1:1000) and mouse anti-ITGB1 AIIB2 (1:100). The following fluorescent conjugated secondary antibodies were used on mouse tissue: goat anti-mouse Alexa Fluor 555 1:500 (Thermo Fisher Scientific), goat anti-chicken 488 1:500 (Aves Labs, Catalog # F-1005), goat anti-Rabbit Alexa Fluor 555 (Thermo Fisher Scientific). To visualize AChR, we used fluorophore conjugated to α-bungarotoxin 1:500 (Thermo Fisher Scientific). When analyzing activated Integrin Beta 1 (anti-ITGB1 9EG7) ± Curarine at the NMJ, we used the post synaptic marker acetylcholine receptors (AChR, fluorophore conjugated a-bungarotoxin) or presynaptic expression of GFP to define a ROI.

**Immunoprecipitation and Western Blot—**20 Larval brains were dissected and ground up in an Eppendorf tube using a pestle in 50 μl of 5X sample buffer and boiled for 10 mins. 10 μl of sample was loaded into and run on a Tris Acetate 3–8% Gel using a Tris-Acetate SDS Running Buffer. Protein was transferred to a nitrocellulose membrane for immunoblotting of Drosophila larval brain whole cell lysates. Mys$^{FLAG}$ (Motor neuron expression using *Gal4*/UAS system), Mys$^{GFP}$, or Mew$^{FLAG}$ were immunoprecipitated (IP) using whole larva cell lysate with anti-Flag or anti-GFP (2μg/μl) and protein G beads in an NP-40 buffer for 2 hours at 4 degrees C. Samples were boiled in sample buffer for 10 min and run on a NuPage 4%–12% or 8% Bis-Tris protein gel (Life Technologies) using a MOPS running buffer. After protein transfer to a nitrocellulose membrane (Bio-Rad), proteins of interest were blotted and anti-B-tubulin was used as a loading control. Band intensities were analyzed with ImageJ. The following antibodies were used for immunoblotting: anti-GFP (mouse, clone N86/8), anti-Integrin beta-PS (mouse, CF.6G11), anti-Talin (mouse, A22A and E16B) anti-B-tubulin (mouse, AA12), Anti-actin (mouse, JLA20), Anti-V5 (Mouse), Anti-c-Myc (rabbit), anti-c-Myc (mouse, 9E 10) and anti-FLAG (mouse,M2). Alexa conjugated secondary antibodies (488, Cy3, Cy5 anti-mouse, anti-rabbit) we used for protein detection in Bio-Rad ChemiDoc imager.

**EM methods—**Larva were fixed with 2% glutaraldehyde in 0.1 M Na cacodylate buffer, pH 7.3, for 2 hours at room temp, rinsed in buffer, and post-fixed with 1% OsO4 in a buffer for 1 hour at room temperature. The post-fixed samples were then rinsed with water, stained *en bloc* with 5% uranyl acetate in water, dehydrated in an ethanol series followed by propylene oxide, and embedded in Eponate 12 resin (Ted Pella, Inc., Redding, CA). 50 nm sections were cut with a Leica UCT ultramicrotome using a Diatome diamond knife, picked up on slot grids with Pioloform films, stained with uranyl acetate and Sato's lead, and examined with an FEI T12 TEM at 120 kV equipped with a Gatan Ultrascan 4k × 4k camera.

**Image acquisition and analysis—**Deconvolution wide field imaging for synapse morphology was performed using a 100x (1.4 NA) plan Apochromat objective (Carl Zeiss) on an Axiovert200 inverted microscope (Carl Zeiss) equipped with a cooled CCD camera (CoolSNAP HQ; Roper Scientific). Image acquisition and analyses were performed in SlideBook software (Intelligent Imaging Innovation). Confocal images were acquired using a Nikon wide field of view spinning disc confocal. This Nikon system uses Andor Zyla sCMOS Camera to collect data. Structured illumination fluorescence microscopy was performed using anN-SIM System (Nikon) with an Apo TIRF 100x/1.49 oil objective on a Ti-E microscope (Nikon) and an Andor DU897 camera. Z stacks of 120 nm step sizes were collected from preparations. Images were reconstructed in NIS-Elements 4.12. Maximum projection images were made.

***Drosophila* NMJ morphology analysis—**Boutons were counted manually on a Zeiss Axioskop 40 compound microscope (40×, 1.1 NA lens). Boutons were quantified for abdominal segments A2. Active zone number was calculated by counting individual BRP puncta (100×, 1.4 NA lens) from maximum intensity projection deconvolved images, using semi-automated routines in Fiji (Wang et al., 2014).

### QUANTIFICATION AND STATISTICAL ANALYSIS

In brief, all bar graphs display data as mean values. The error bars represent SEM. In most cases, a One-way Anova with Tukey correction for multiple comparisons was used, comparing data across multiple experimental groups. This includes statistical tests of genotypes in the presence or absence of the PHP induction. Occasionally, as specifically indicated in figure legends, a Students t-test was used to make comparisons between experimental and control comprised of only two groups (unpaired; two-tailed). All statistical details for comparison can be found in the figure legends. Sample sizes are reported directly on graphs or within figure legends. Experimental sample sizes equal to or greater than 6 were considered sufficiently powered to detect a significant change between groups, an effect of size of ~80–120% compared to controls. Therefore, our sample of 8 recordings or more surpassed the sample sized required to detect a significant change between groups. Synaptic Talin puncta were quantified using the GA3 AI software (Nikon). The parameters in which we quantified the synaptic (BRP associated) Talin protein are as follows: Synaptic BRP signal was used as a mask to identify synaptic Talin protein. The program analyzed all colocalized (within 120 nm of BRP) Talin structures. The software assembled and reconstructed all Talin structures that met this colocalization requirement, analyzing their spatial features. Comparisons were made between synaptic Talin structures in the absence versus the presence of PhTx.

## Supplementary Material

Refer to Web version on PubMed Central for supplementary material.

## ACKNOWLEDGEMENTS

Supported by NINDS grant number R35NS097212 to GWD

# REFERENCES

Babayan AH, Kramár EA, Barrett RM, Jafari M, Häettig J, Chen LY, Rex CS, Lauterborn JC, Wood MA, Gall CM, & Lynch G (2012). Integrin dynamics produce a delayed stage of long-term potentiation and memory consolidation. Journal of Neuroscience, 32, 12854–12861. 10.1523/JNEUROSCI.2024-12.2012. [PubMed: 22973009]

Berginski ME, Vitriol EA, Hahn KM, & Gomez SM (2011). High-resolution quantification of focal adhesion spatiotemporal dynamics in living cells. PLoS ONE, 6, e22025. 10.1371/journal.pone.0022025. [PubMed: 21779367]

Beumer KJ, Rohrbough J, Prokop A, & Broadie K (1999). A role for PS integrins in morphological growth and synaptic function at the postembryonic neuromuscular junction of Drosophila. Development, 126, 5833–5846. 10.1242/dev.126.24.5833. [PubMed: 10572057]

Bleckert A, Photowala H, & Alford S (2012). Dual pools of actin at presynaptic terminals. Journal of Neurophysiology, 107, 3479–3492. 10.1152/jn.00789.2011. [PubMed: 22457456]

Broadie K, Baumgartner S, & Prokop A (2011). Extracellular matrix and its receptors in drosophila neural development. Developmental Neurobiology, 71, 1102–1130. 10.1002/dneu.20935. [PubMed: 21688401]

Brusich DJ, Spring AM, & Frank CA (2015). A single-cross, RNA interference-based genetic tool for examining the long-term maintenance of homeostatic plasticity. Frontiers in cellular neuroscience, 9, 107. 10.3389/fncel.2015.00107. [PubMed: 25859184]

Bunch TA, Salatino R, Engelsgjerd MC, Mukai L, West RF, & Brower DL (1992). Characterization of mutant alleles of myospheroid, the gene encoding the β subunit of the Drosophila PS integrins. Genetics, 132, 519–528. 10.1093/genetics/132.2.519. [PubMed: 1427041]

Byron A, Humphries JD, Askari JA, Craig SE, Mould AP, & Humphries MJ (2009). Anti-integrin monoclonal antibodies. Journal of Cell Science, 122, 4009–4011. 10.1242/jcs.056770. [PubMed: 19910492]

Carulli D, de Winter F, & Verhaagen J (2021). Semaphorins in Adult Nervous System Plasticity and Disease. Frontiers in synaptic neuroscience, 13, 672891. 10.3389/fnsyn.2021.672891. [PubMed: 34045951]

Chan CS, Weeber EJ, Zong L, Fuchs E, Sweatt JD, & Davis RL (2006). β1-integrins are required for hippocampal AMPA receptor-dependent synaptic transmission, synaptic plasticity, and working memory. Journal of Neuroscience, 26, 223–232. 10.1523/JNEUROSCI.4110-05.2006. [PubMed: 16399691]

Chenouard N, Xuan F, & Tsien RW (2020). Synaptic vesicle traffic is supported by transient actin filaments and regulated by PKA and NO. Nature Communications, 11, 5318. 10.1038/s41467-020-19120-1.

Cingolani LA, Thalhammer A, Yu LMY, Catalano M, Ramos T, Colicos MA, & Goda Y (2008). Activity-Dependent Regulation of Synaptic AMPA Receptor Composition and Abundance by β3 Integrins. Neuron, 58, 749–762. 10.1016/j.neuron.2008.04.011. [PubMed: 18549786]

Davis GW (2006). Homeostatic control of neural activity: From phenomenology to molecular design. Annual review of neuroscience, 29, 307–323. 10.1146/annurev.neuro.28.061604.135751

Davis GW (2013). Homeostatic signaling and the stabilization of neural function. Neuron, 80, 718–728. 10.1016/j.neuron.2013.09.044. [PubMed: 24183022]

Delvendahl I, Kita K, & Müller M (2019). Rapid and sustained homeostatic control of presynaptic exocytosis at a central synapse. PNAS, 116, 23783–23789. 10.1073/pnas.1909675116. [PubMed: 31685637]

Delvendahl I, & Müller M (2019). Homeostatic plasticity—a presynaptic perspective. Current opinion in neurobiology, 54, 155–162. 10.1016/j.conb.2018.10.003. [PubMed: 30384022]

Dickman DK, & Davis GW (2009). The schizophrenia susceptibility gene dysbindin controls synaptic homeostasis. Science, 326, 1127–1130. 10.1126/science.1179685. [PubMed: 19965435]

Ehmann N, Van De Linde S, Alon A, Ljaschenko D, Keung XZ, Holm T, Rings A, DiAntonio A, Hallermann S, Ashery U, Heckmann M, Sauer M, & Kittel RJ (2014). Quantitative super-resolution imaging of Bruchpilot distinguishes active zone states. Nature Communications, 5, 4650. 10.1038/ncomms5650.

Eitzen G (2003). Actin remodeling to facilitate membrane fusion. Biochimica et Biophysica Acta - Molecular Cell Research, 1641, 175–181. 10.1016/s0167-4889(03)00087-9.

Ellis SJ, Pines M, Fairchild MJ, & Tanentzapf G (2011). In vivo functional analysis reveals specific roles for the integrin-binding sites of talin. Journal of Cell Science, 124, 1844–1856. 10.1242/jcs.083337. [PubMed: 21558413]

Frank CA, Kennedy MJ, Goold C, Marek KW, & Davis G (2006). Mechanisms Underlying the Rapid Induction and Sustained Expression of Synaptic Homeostasis. Neuron, 52, 663–677. 10.1016/j.neuron.2006.09.029. [PubMed: 17114050]

Frank CA, Pielage J, & Davis GW (2009). A Presynaptic Homeostatic Signaling System Composed of the Eph Receptor, Ephexin, Cdc42, and CaV2.1 Calcium Channels. Neuron, 61, 556–569. 10.1016/j.neuron.2006.09.029. [PubMed: 19249276]

Frere S, & Slutsky I (2018). Alzheimer's Disease: From Firing Instability to Homeostasis Network Collapse. Neuron, 97, 32–58. 10.1016/j.neuron.2017.11.028. [PubMed: 29301104]

Genç Ö, An J-Y, Fetter RD, Kulik Y, Zunino G, Sanders SJ, & Davis GW (2020). Homeostatic plasticity fails at the intersection of autism-gene mutations and a novel class of common genetic modifiers. ELife, 9. 10.7554/eLife.55775.

Genç Ö, & Davis GW (2019). Target-wide Induction and Synapse Type-Specific Robustness of Presynaptic Homeostasis. Current Biology, 29, 3863–3873.e2 10.1016/j.cub.2019.09.036. [PubMed: 31708391]

Goold CP, & Davis GW (2007). The BMP Ligand Gbb Gates the Expression of Synaptic Homeostasis Independent of Synaptic Growth Control. Neuron, 56, 109–123 10.1016/j.neuron.2007.08.006. [PubMed: 17920019]

Grabbe C, Zervas CG, Hunter T, Brown NH, & Palmer RH (2004). Focal adhesion kinase is not required for integrin function or viability in Drosophila. Development, 131, 5795–5805. 10.1242/dev.01462. [PubMed: 15525665]

Hall DE, Reichardt LF, Crowley E, Holley B, Moezzi H, Sonnenberg A, & Damsky CH (1990). The α1/β1 and α6/β1 integrin heterodimers mediate cell attachment to distinct sites on laminin. Journal of Cell Biology, 110, 2175–2184. 10.1083/jcb.110.6.2175. [PubMed: 2351695]

Harris N, Fetter RD, Brasier DJ, Tong A, & Davis GW (2018). Molecular Interface of Neuronal Innate Immunity, Synaptic Vesicle Stabilization, and Presynaptic Homeostatic Plasticity. Neuron, 100, 1163–1179.e4. 10.1016/j.neuron.2018.09.048. [PubMed: 30344041]

Houtman JCD, Barda-Saad M, & Samelson LE (2005). Examining multiprotein signaling complexes from all angles: The use of complementary techniques to characterize complex formation at the adapter protein, linker for activation of T cells. FEBS Journal, 272, 5426–5435. 10.1111/j.1742-4658.2005.04972. [PubMed: 16262684]

Huttenlocher A, & Horwitz AR (2011). Integrins in cell migration. Cold Spring Harbor perspectives in biology, 3, a005074. 10.1101/cshperspect.a005074. [PubMed: 21885598]

Janssen BJC, Malinauskas T, Weir GA, Cader MZ, Siebold C, & Jones EY (2012). Neuropilins lock secreted semaphorins onto plexins in a ternary signaling complex. Nature Structural and Molecular Biology, 19, 1293–1299. 10.1038/nsmb.2416.

Johnson AE, Orr BO, Fetter RD, Moughamian AJ, Primeaux LA, Geier EG, Yokoyama JS, Miller BL, & Davis GW (2021). SVIP is a molecular determinant of lysosomal dynamic stability, neurodegeneration and lifespan. Nature Communications, 12, 513. 10.1038/s41467-020-20796-8.

Klapholz B, & Brown NH (2017). Talin - The master of integrin adhesions. Journal of Cell Science, 130, 2435–2446. 0.1242/jcs.190991. [PubMed: 28701514]

Lenter M, Uhlig H, Hamann A, Jeno P, Imhof B, & Vestweber D (1993). A monoclonal antibody against an activation epitope on mouse integrin chain β1 blocks adhesion of lymphocytes to the endothelial integrin α6β1. PNAS, 90, 9051–9055. 10.1073/pnas.90.19.9051. [PubMed: 7692444]

Li R, Mitra N, Gratkowski H, & Vilaire G (2003). Activation of integrin alphaIIbbeta3 by modulation of transmembrane helix associations. Science, 300, 795–798. 10.1126/science.1079441. [PubMed: 12730600]

Lin B, Arai AC, Lynch G, & Gall CM (2003). Integrins regulate NMDA receptor-mediated synaptic currents. Journal of Neurophysiology, 89, 2874–2878. 10.1152/jn.00783.2002. [PubMed: 12740418]

Luo BH, Karanicolas J, Harmacek LD, Baker D, & Springer TA (2009). Rationally designed integrin β3 mutants stabilized in the high affinity conformation. Journal of Biological Chemistry. 284, 3917–3924. 10.1074/jbc.M806312200. [PubMed: 19019827]

Maschi D, Gramlich MW, & Klyachko VA (2018). Myosin V functions as a vesicle tether at the plasma membrane to control neurotransmitter release in central synapses. ELife, 7, e39440. 10.7554/eLife.39440. [PubMed: 30320552]

Meltzer S, Yadav S, Lee J, Soba P, Younger SH, Jin P, Zhang W, Parrish J, Jan LY, & Jan YN (2016). Epidermis-Derived Semaphorin Promotes Dendrite Self-Avoidance by Regulating Dendrite-Substrate Adhesion in Drosophila Sensory Neurons. Neuron, 89, 741–755. 10.1016/j.neuron.2016.01.020. [PubMed: 26853303]

Michael M, & Parsons M (2020). New perspectives on integrin-dependent adhesions. Current Opinion in Cell Biology, 63, 31–37. 10.1016/j.ceb.2019.12.008. [PubMed: 31945690]

Miteva A, Gaydukov A, & Balezina O (2020). Interaction between Calcium Chelators and the Activity of P2X7 Receptors in Mouse Motor Synapses. International journal of molecular sciences, 21, 2034. 10.3390/ijms21062034.

Morales M, Colicos MA, & Goda Y (2000). Actin-dependent regulation of neurotransmitter release at central synapses. Neuron, 27, 539–550. 10.1016/s0896-6273(00)00064-7. [PubMed: 11055436]

Morgan JR, Di Paolo G, Werner H, Shchedrina VA, Pypaert M, Pieribone VA, & De Camilli P (2004). A role for talin in presynaptic function. Journal of Cell Biology, 167, 43–50. 10.1083/jcb.200406020. [PubMed: 15479735]

Müller M, Genç O, & Davis GW (2015). RIM-binding protein links synaptic homeostasis to the stabilization and replenishment of high release probability vesicles. Neuron, 85, 1056–1069. 10.1016/j.neuron.2015.01.024. [PubMed: 25704950]

Müller M, Liu KSY, Sigrist SJ, & Davis GW (2012). RIM controls homeostatic plasticity through modulation of the readily-releasable vesicle pool. Journal of Neuroscience, 32, 16574–16585. 10.1523/JNEUROSCI.0981-12.2012. [PubMed: 23175813]

Mullins C, Fishell G, & Tsien RW (2016). Unifying Views of Autism Spectrum Disorders: A Consideration of Autoregulatory Feedback Loops. Neuron 89, 1131–1156. 10.1016/j.neuron.2016.02.017. [PubMed: 26985722]

Munger JS, & Sheppard D (2011). Cross talk among TGF-β signaling pathways, integrins, and the extracellular matrix. Cold Spring Harbor Perspectives in Biology, 3, a005017. 10.1101/cshperspect.a005017. [PubMed: 21900405]

Nagarkar-Jaiswal S, Manivannan SN, Zuo Z, & Bellen HJ (2017). A cell cycle-independent, conditional gene inactivation strategy for differentially tagging wild-type and mutant cells. eLife, 6, e26420. 10.7554/eLife.26420. [PubMed: 28561736]

Nishimune H, Valdez G, Jarad G, Moulson CL, Müller U, Miner JH, & Sanes JR (2008). Laminins promote postsynaptic maturation by an autocrine mechanism at the neuromuscular junction. Journal of Cell Biology, 182, 1201–1215. 10.1083/jcb.200805095. [PubMed: 18794334]

Orr BO, Fetter RD, & Davis GW (2017). Retrograde semaphorin-plexin signalling drives homeostatic synaptic plasticity. Nature, 550, 109–113. 10.1038/nature24017. [PubMed: 28953869]

Orr BO, Hauswirth AG, Celona B, Fetter RD, Zunino G, Kvon EZ, Zhu Y, Pennacchio LA, Black BL, & Davis GW (2020). Presynaptic Homeostasis Opposes Disease Progression in Mouse Models of ALS-Like Degeneration: Evidence for Homeostatic Neuroprotection. Neuron, 107, 95–111.e6. 10.1016/j.neuron.2020.04.009. [PubMed: 32380032]

Ortega JM, Genç Ö, & Davis GW (2018). Molecular mechanisms that stabilize short term synaptic plasticity during presynaptic homeostatic plasticity. eLife, 7, e40385. 10.7554/eLife.40385. [PubMed: 30422113]

Papadopulos A, Tomatis VM, Kasula R, & Meunier FA (2013). The Cortical Acto-Myosin Network: From Diffusion Barrier to Functional Gateway in the Transport of Neurosecretory Vesicles to the Plasma Membrane. Frontiers in endocrinology, 4, 153. 10.3389/fendo.2013.00153. [PubMed: 24155741]

Park YK, & Goda Y (2016). Integrins in synapse regulation. Nature Reviews Neuroscience, 17, 745–756. 10.1038/nrn.2016.138. [PubMed: 27811927]

Pascoe HG, Wang Y, & Zhang X (2015). Structural mechanisms of plexin signaling. Progress in Biophysics and Molecular Biology, 118, 161–168. 10.1016/j.pbiomolbio.2015.03.006. [PubMed: 25824683]

Pielage J, Fetter RD, & Davis GW (2005). Presynaptic spectrin is essential for synapse stabilization. Current biology : CB, 15, 918–928. 10.1016/j.cub.2005.04.030. [PubMed: 15916948]

Pines M, Fairchild MJ, & Tanentzapf G (2011). Distinct regulatory mechanisms control integrin adhesive processes during tissue morphogenesis. Developmental Dynamics, 240, 36–51. 10.1002/dvdy.22488. [PubMed: 21089076]

Plomp JJ, van Kempen GT, & Molenaar PC (1992a). Adaptation of quantal content to decreased postsynaptic sensitivity at single endplates in alpha-bungarotoxin-treated rats. The Journal of physiology, 458, 487–499. 10.1113/jphysiol.1992.sp019429. [PubMed: 1302275]

Raghavan S, Bauer C, Mundschau G, Li Q, & Fuchs E (2000). Conditional ablation of β1 integrin in skin: Severe defects in epidermal proliferation, basement membrane formation, and hair follicle invagination. Journal of Cell Biology, 150, 1149–1160. 10.1083/jcb.150.5.1149. [PubMed: 10974002]

Rohrbough J, Grotewiel MS, Davis RL, & Broadie K (2000). Integrin-mediated regulation of synaptic morphology, transmission, and plasticity. Journal of Neuroscience, 20, 6868–6878. 10.1523/JNEUROSCI.20-18-06868.2000. [PubMed: 10995831]

Roman G, & Davis RL (2001). Molecular biology and anatomy of Drosophila olfactory associative learning. BioEssays, 23, 571–581. 10.1002/bies.1083. [PubMed: 11462211]

Ross JA, Webster RG, Lechertier T, Reynolds LE, Turmaine M, Bencze M, Jamshidi Y, Cetin H, Muntoni F, Beeson D, Hodilvala-Dilke K, & Conti FJ (2017). Multiple roles of integrin-α3 at the neuromuscular junction. Journal of Cell Science, 130, 1772–1784. 0.1242/jcs.201103. [PubMed: 28386022]

Sankaranarayanan S, Atluri PP, & Ryan TA (2003). Actin has a molecular scaffolding, not propulsive, role in presynaptic function. Nature Neuroscience, 6, 127–135. 10.1038/nn1002. [PubMed: 12536209]

Schlaepfer DD, Hauck CR, & Sieg DJ (1999). Signaling through focal adhesion kinase. Progress in Biophysics and Molecular Biology, 71, 435–478. 10.1016/s0079-6107(98)00052-2. [PubMed: 10354709]

Schneggenburger R, & Neher E (2005). Presynaptic calcium and control of vesicle fusion. Current Opinion in Neurobiology, 15, 266–274. 10.1016/j.conb.2005.05.006. [PubMed: 15919191]

Schwander M, Shirasaki R, Pfaff SL, & Müller U (2004). Β1 Integrins in Muscle, But Not in Motor Neurons, Are Required for Skeletal Muscle Innervation. Journal of Neuroscience, 24, 8181–8191. 10.1523/JNEUROSCI.1345-04.2004. [PubMed: 15371519]

Terman JR, Mao T, Pasterkamp RJ, Yu HH, & Kolodkin AL (2002). MICALs, a Family of Conserved Flavoprotein Oxidoreductases, Function in Plexin-Mediated Axonal Repulsion. Cell, 109, 887–900. 10.1016/s0092-8674(02)00794-8. [PubMed: 12110185]

Tsai PI, Kao HH, Grabbe C, Lee YT, Ghose A, Lai TT, Peng KP, Van Vactor D, Palmer RH, Chen RH, Yeh SR, & Chien CT (2008). Fak56 functions downstream of integrin alphaPS3betanu and suppresses MAPK activation in neuromuscular junction growth. Neural development, 3, 26. 0.1186/1749–8104-3–26. [PubMed: 18925939]

Wagh DA, Rasse TM, Asan E, Hofbauer A, Schwenkert I, Dürrbeck H, Buchner S, Dabauvalle MC, Schmidt M, Qin G, Wichmann C, Kittel R, Sigrist SJ, & Buchner E (2006). Bruchpilot, a protein with homology to ELKS/CAST, is required for structural integrity and function of synaptic active zones in Drosophila. Neuron, 49, 833–844. 10.1016/j.neuron.2006.02.008. [PubMed: 16543132]

Wang J, & Richards DA (2011). Spatial regulation of exocytic site and vesicle mobilization by the actin cytoskeleton. PloS one, 6, e29162. 10.1371/journal.pone.0029162. [PubMed: 22195014]

Wang Q, Chiu SL, Koropouli E, Hong I, Mitchell S, Easwaran TP, Hamilton NR, Gustina AS, Zhu Q, Ginty DD, Huganir RL, & Kolodkin AL (2017). Neuropilin-2/PlexinA3 Receptors Associate with GluA1 and Mediate Sema3F-Dependent Homeostatic Scaling in Cortical Neurons. Neuron, 96, 1084–1098.e7. 10.1016/j.neuron.2017.10.029. [PubMed: 29154130]

Wang T, Morency DT, Harris N, & Davis GW (2020). Epigenetic Signaling in Glia Controls Presynaptic Homeostatic Plasticity. Neuron, 105, 491–505.e3. 10.1016/j.neuron.2019.10.041. [PubMed: 31810838]

Wang T, Hauswirth AG, Tong A, Dickman DK, & Davis GW (2014). Endostatin Is a Trans-Synaptic Signal for Homeostatic Synaptic Plasticity. Neuron, 83, 616–629. 10.1016/j.neuron.2014.07.003. [PubMed: 25066085]

Wang X, Pinter MJ, & Rich MM (2016). Reversible Recruitment of a Homeostatic Reserve Pool of Synaptic Vesicles Underlies Rapid Homeostatic Plasticity of Quantal Content. J Neurosci, 36, 828–836. 10.1523/JNEUROSCI.3786-15.2016. [PubMed: 26791213]

Webb DJ, Donais K, Whitmore LA, Thomas SM, Turner CE, Parsons JT, & Horwitz AF (2004). FAK-Src signalling through paxillin, ERK and MLCK regulates adhesion disassembly. Nature Cell Biology, 6, 154–161. 10.1038/ncb1094. [PubMed: 14743221]

Weyhersmüller A, Hallermann S, Wagner N, & Eilers J (2011). Rapid active zone remodeling during synaptic plasticity. Journal of Neuroscience, 31, 6041–6052. 10.1523/JNEUROSCI.6698-10.2011. [PubMed: 21508229]

Wu H, Yesilyurt HG, Yoon J, & Terman JR (2018). The MICALs are a Family of F-actin Dismantling Oxidoreductases Conserved from Drosophila to Humans. Scientific reports, 8, 937. 10.1038/s41598-017-17943-5. [PubMed: 29343822]

Younger M, Müller M, Tong A, Pym E, & Davis G (2013). A presynaptic ENaC channel drives homeostatic plasticity. Neuron, 79, 1183–1196. 10.1016/j.neuron.2013.06.048. [PubMed: 23973209]

Yu H-H, & Kolodkin AL (1999). Semaphorin Signaling: a little less per-plexin. Neuron, 22, 11–14. 10.1016/s0896-6273(00)80672-8. [PubMed: 10027283]

## HIGHLIGHTS:

1. Beta-Integrin drives presynaptic homeostatic plasticity (PHP) in mouse and *Drosophila*.
2. Beta-Integrin is a presynaptic PlexinB co-receptor that is necessary for PHP.
3. Expansion of a presynaptic complex of Sema2b, PlexB, Talin and FAK drives PHP.
4. A model includes signaling convergence and a dynamic presynaptic molecular assembly.

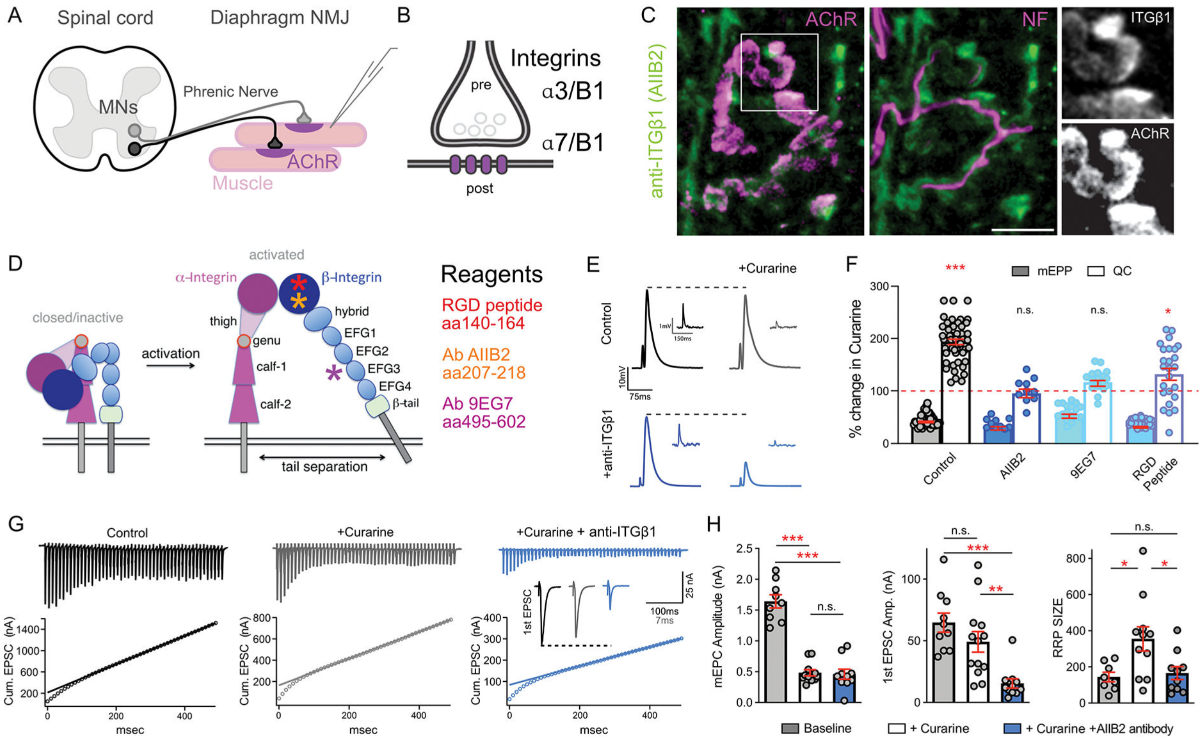

**Figure 1. Acute ITGB1 antagonism blocks PHP**

**A)** Diagram of recording configuration at the diaphragm NMJ. **B)** alpha/beta-Integrin dimers at the NMJ. **C)** Anti-ITGβ1 (Ab AIIB2, green) at the NMJ co-localizes with postsynaptic (AChR, left magenta) and presynaptic Neurofilament (middle magenta). Scale 10 μm. Inset at right. **D)** alpha/beta-Integrin dimer activation. Asterisks indicate the approximate binding of function blocking reagents. **E)** Representative traces (EPP and mEPP) for indicated treatments. **F)** All recording are in the presence of beta-Integrin inhibitors. Data displayed as percent change for mEPP amplitude (mEPP, filled bars) and quantal content (QC, open bars) in the presence versus absence of Curarine. **G)** Representative two-electrode voltage clamp traces for indicated pharmacological treatments. Bottom graph presents back extrapolation to Y axis for RRP estimation. **H)** Average data for voltage clamp recordings. Data represent mean ± SEM. One-way Anova with Tukey correction for multiple comparisons; $*p < 0.05$, $**p < 0.01$, $***p < 0.001$. n.s., not significant. Recordings 2 mM $[Ca^{2+}]_e$. Supplemental Figure 1 for non-normalized values.

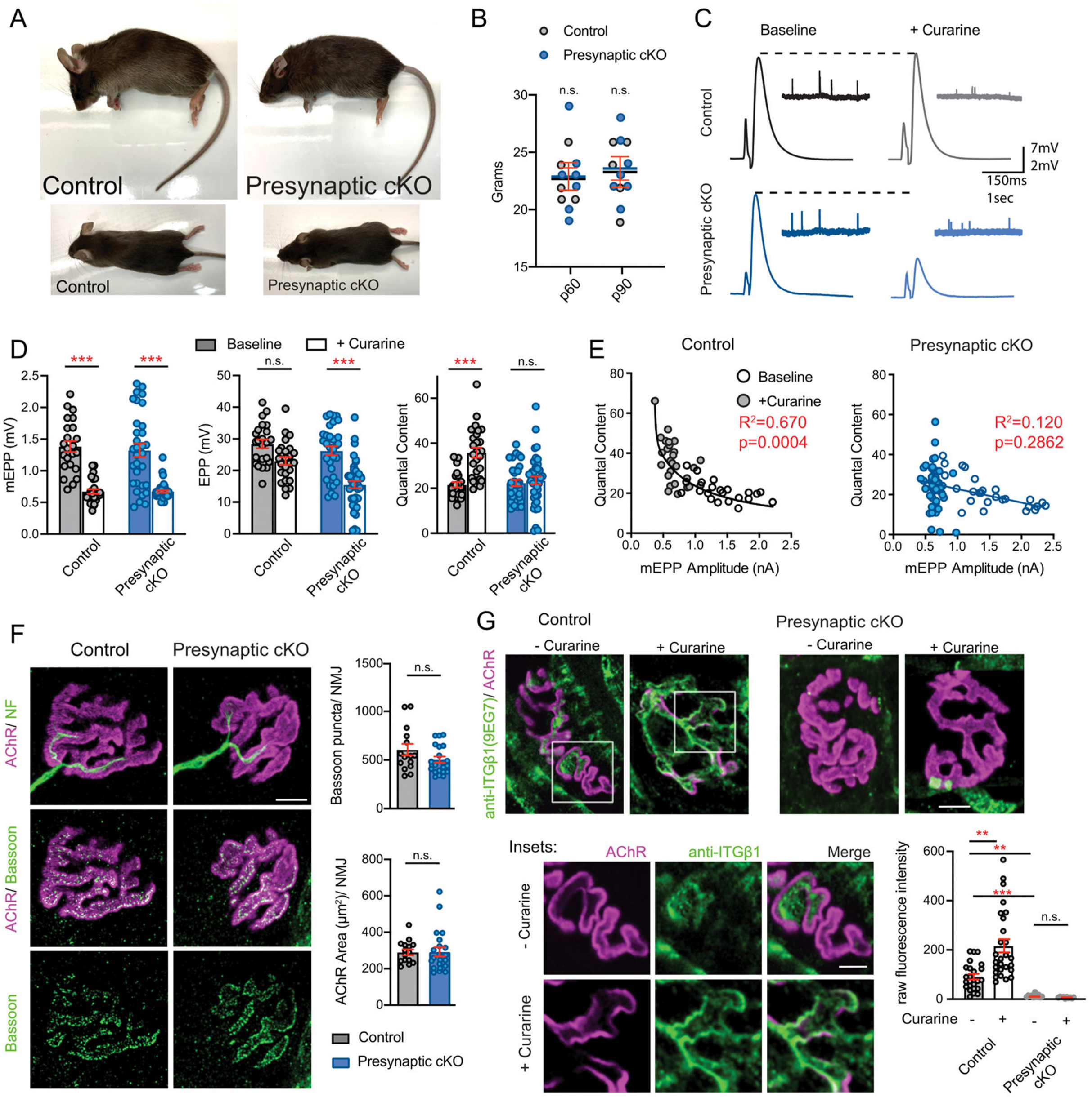

**Figure 2. Presynaptic ITGB1 is essential for PHP and redistributes during PHP**

**A)** Images of control (*HB9*$^{+/+}$*; Itgb1* $^{loxP/loxP}$) and *ITGB1* conditional knockout in motoneurons (cKO) (*HB9*$^{Cre/+}$*; Itgb1* $^{loxP/loxP}$) animals. **B)** Weights at p60 and p90 are not different. **C)** Representative traces for indicated genotypes and treatments. **D)** Average data for NMJ recordings as in (C) (animal number: 4 cKO and 2 controls). **E)** NMJ recordings for indicated genotypes in the absence (baseline, open circle) and presence of curarine (+Curarine; filled circle). Control NMJs demonstrate a strong negative correlation. ITGB1 presynaptic cKO disrupts the negative correlation. **F)** Representative images of NMJs for indicated genotypes labeled as indicated. Scale bar 10µm. Graphs at right report averaged Bassoon puncta number or AChR area per NMJ. **G)** Representative images of NMJs labeled for activated ITGB1 (Ab 9EG7, green) for indicated genotypes, treatments and staining. Scale bar, 10µm. Quantification at right. Postsynaptic AChR staining was used as a mask to identify and quantify ITGB1 present at the endplate. Inset scale bar is 5µm. Data represent mean ± SEM. Significance determined by One-way Anova with Tukey correction for multiple comparisons. Student's t-test used in graphs containing only two bars; $*p < 0.05$, $**p < 0.01$, $***p < 0.001$. n.s., not significant. Recordings at 2 mM $[Ca^{2+}]_e$.

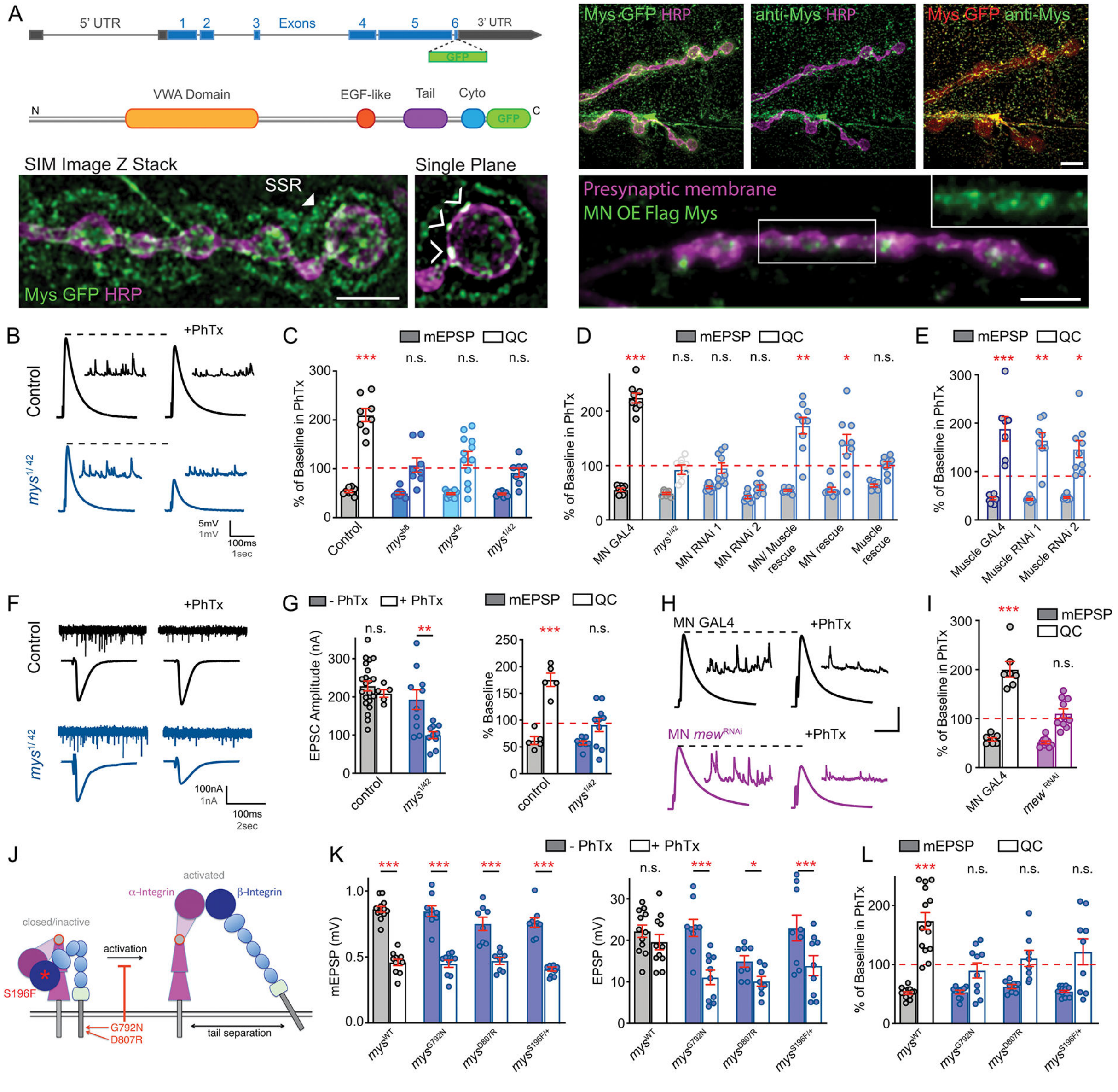

**Figure 3. Synaptic alpha/beta-Integrin is necessary for PHP in *Drosophila***

**A**) Schematic of CRISPR directed GFP Tag insertion after exon six in the *mys* locus (DNA top, protein bottom). Image below shows SIM image (2D projection) of Mys$^{GFP}$ (green) and a presynaptic membrane marker (HRP, magenta). Arrowhead indicates SSR. Inset at right is a single plane with membrane co-localized Mys$^{GFP}$ indicated (white arrowheads). Right (top three panels) show Mys$^{GFP}$ (Red) co-localizing with anti-Mys (Ab CF.6G11) antibody (green). Bottom panel demonstrates that motoneuron over-expressed Mys$^{FLAG}$ protein traffics to the presynaptic terminal. All scale bars are 5 µm. **B)** Representative traces for (mEPSPs and EPSPs) of indicated genotypes and treatments. **C)** Normalized data displayed as percent change in the presence versus absence of PhTx. **D)** Data as in (C). Motor neuron (MN) *Gal4* (*OK371-Gal4*) is used as control. **E)** Data as in (C). Muscle *Gal4* (*BG57-Gal4*) is the control. **F)** Representative traces, voltage clamp recordings in 1 mM [Ca2+]$_e$. **G)** Averaged data (left) and normalized data as in (C). **H)** Representative current clamp traces. **I)** Data as in (C). Control is *OK371- Gal4*. **J)** Diagram of *mys* mutations and inhibition of Integrin activation. **K)** Averaged data for NMJ recordings. **L)** Normalized data (from K) displayed as in (C). Data presented as mean ± SEM. Significance determined by One-way Anova with Tukey correction for multiple comparisons; $*p < 0.05$, $**p < 0.01$, $***p < 0.001$. n.s., not significant. Recordings at 0.3 mM $[Ca2+]_{e,}$ unless otherwise indicated in the figure. Refer to Supplemental Figures 2,3, and for non-normalized values.

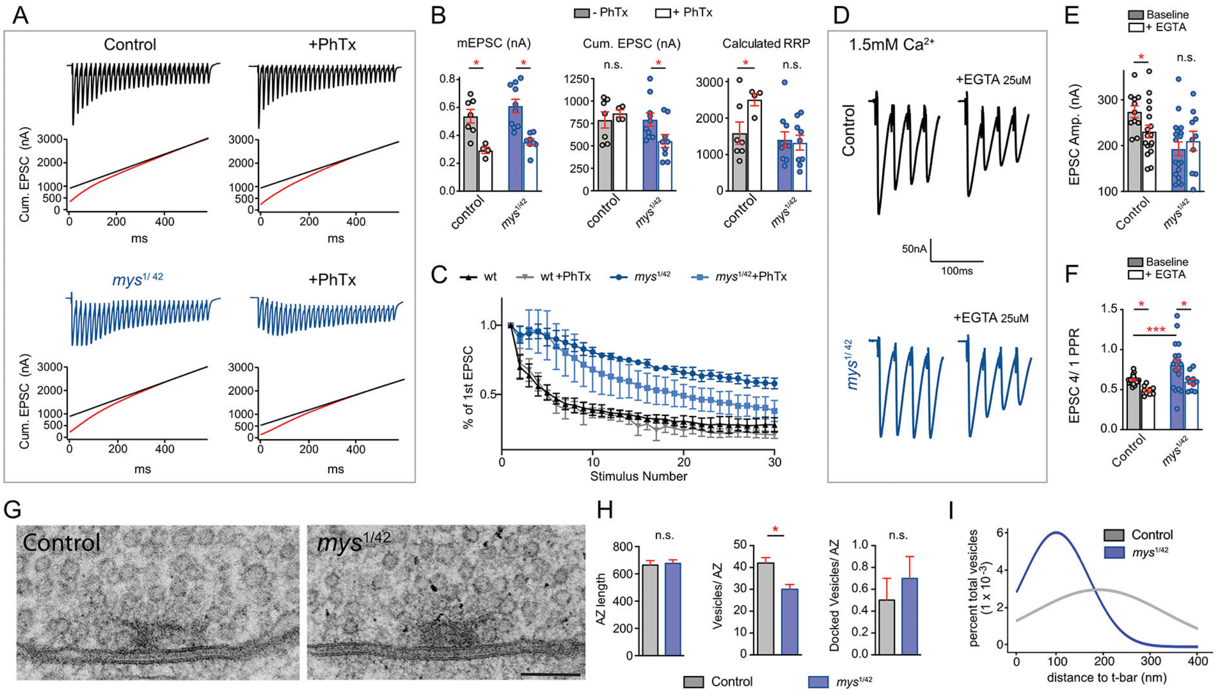

**Figure 4. Beta-Integrin is necessary for PHP-dependent potentiation of the RRP**

**A)** Representative voltage clamp traces and back extrapolations (graphs) for individual recordings. Data from control (black) and *mys* mutant (+/− PhTx) (60 Hz stimulation). **B)** Averaged data for genotypes in (A). **C)** Average EPSC amplitudes normalized to the first stimulus of each train, plotted as stimulus number. **D)** Representative EPSC traces at baseline and following incubation in EGTA-AM (25 mM, 10min) for indicated genotypes. **E)** Average data for first EPSC amplitudes for data as in (D). **F)** Average data for EPSC4/ EPSC1, ± EGTA-AM. **G)** Representative electron micrographs of presynaptic active zones for indicated genotypes (scale bar 100nm. **H)** Average data for active zone length, vesicle number (within 150 nm of the base of the T-bar) and docked vesicles/NMJ. **I)** Docked vesicle distribution plotted as percent of total vesicles within 400 nm of the T-bar base. Averaged data are mean ± SEM. Significance determined by One-way Anova with Tukey correction for multiple comparisons. Student's t-test used in graphs containing only two bars; *p < 0.05, **p < 0.01, ***p < 0.001. n.s., not significant. Recordings at 1.5 mM $[Ca^{2+}]_e$.

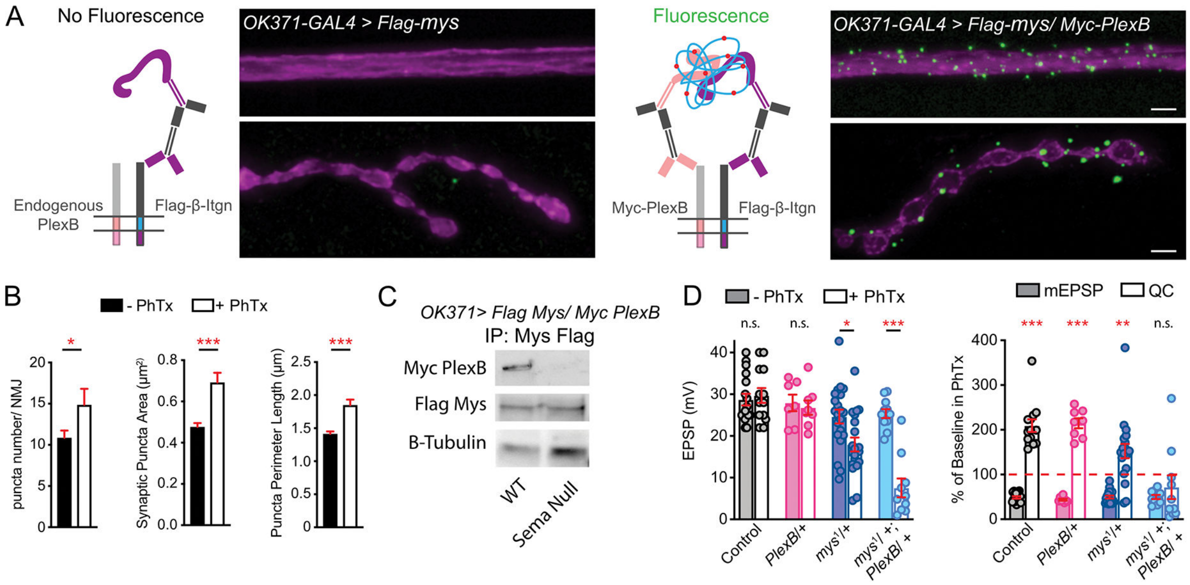

**Figure 5. Biochemical Interaction of beta-Integrin and PlexinB**

**A**) Diagram and images for proximity ligation assay (PLA) between motoneuron over-expressed Mys (*flag-mys*) and PlexinB (*myc-PlexB*) (*OK371-Gal4* driver) (scale 5μm). No reaction is observed in control (*OK371-Gal4*, left). **B)** Quantification of PLA puncta number, area, and perimeter (+/−PhTx). Mann-Whitney U-test, * p=0.05, *** p<0.001; n>20 NMJ per condition. **C)** Western blot of myc-PlexB and flag-Mys. *UAS-myc-PlexB* and *UAS-flag-mys* (*OK371-Gal4* driver) in wild type or *sema2b* null animals. Flag-Mys was immunoprecipitated from both genotypes. **D)** Averaged EPSP and normalized data (mEPSP and quantal content) for indicated genotypes. Averaged data represent mean ± SEM. Significance (panel D) determined by One-way Anova with Tukey correction for multiple comparisons; *p < 0.05, **p < 0.01, ***p < 0.001. n.s., not significant. Recordings at 0.3 mM [Ca2+]$_e$. Refer to Supplemental Figure 5 for non-normalized data.

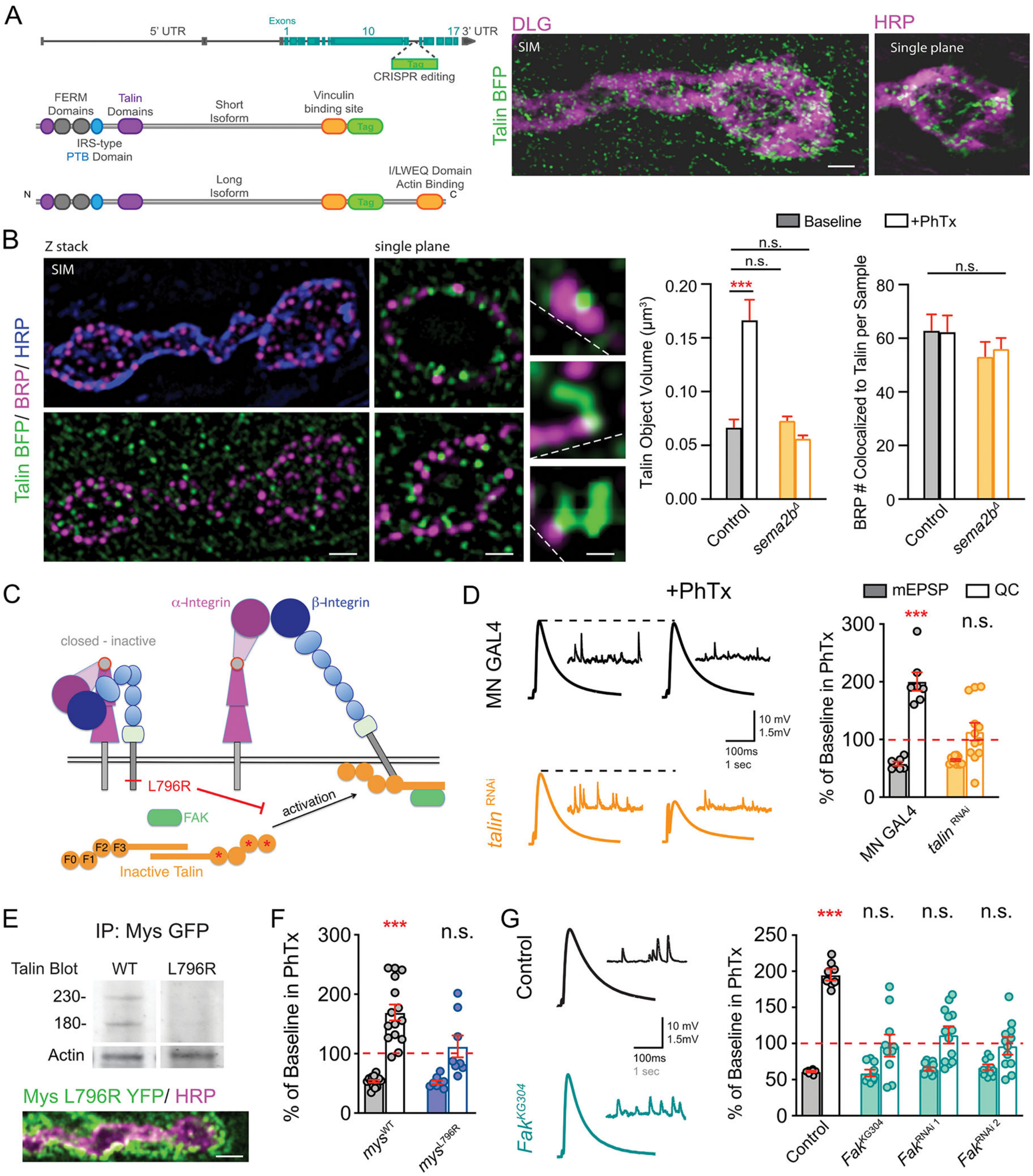

**Figure 6. Presynaptic Talin participation and rearrangement during PHP**

**A)** Schematic of CRISPR-tagged Talin$^{BFP,Myc}$ inserted between exons 11 and 12. Images to the right show SIM of Talin$^{BFP}$ (green) and DLG (magenta) or HRP (Magenta) (scale 3 μm). **B)** SIM images demonstrating BRP (magenta) localization at the presynaptic membrane (HRP, blue) and Talin$^{BFP}$ (green) distribution at BRP labeled active zones. Dotted lines in high magnification images of single active zones delineate presynaptic plasma membrane position and orientation. Averaged data for Talin object volumes that co-localize with BRP in the presence (+PhTx) or absence of PhTx (Baseline). Far right: average of BRP objects that co-localize with Talin (±PhTx). Scale bars are 5 μm, 3 μm and 1 μm (left to right). **C)** Diagram of *mys* mutation (*L796R*) effect. **D)** Representative current clamp traces (±PhTx). Data displayed as percent change (±PhTx). *OK371-Gal4* is the control genotype. **E)** Western blot of Talin protein (anti-Talin A22A and E16B antibodies) from immunoprecipitation of Ubi:Mys$^{YFP}$ or Ubi:Mys$^{YFP\ L796R}$. Actin serves as loading control. Image of Mys$^{YFP\ L796R}$ (Green) at the synaptic terminal (HRP, magenta). Scale Bar is 5 μm. **F)** Normalized data for recordings of indicated genotypes. Data displayed as percent change (±PhTx). **G)** Representative traces. Data displayed as percent change (±PhTx). Averaged data represent mean ± SEM. Significance determined by One-way Anova with Tukey correction for multiple comparisons. Student's t-test used in graphs containing only two bars; *p < 0.05, **p < 0.01, ***p < 0.001. n.s., not significant. Recordings at 0.3 mM $[Ca2+]_e$. Refer to Supplemental Figure 7 for non-normalized data.

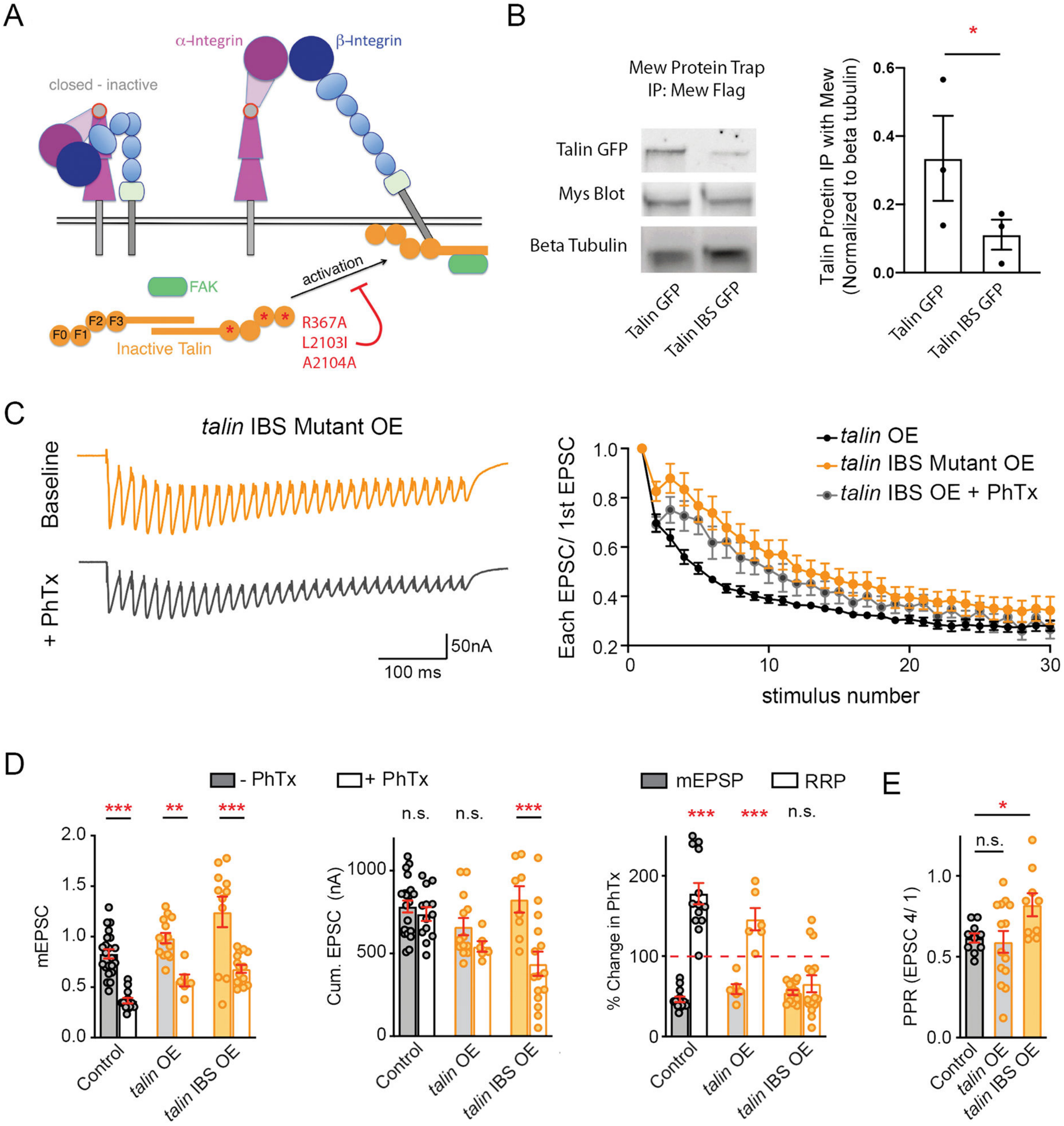

**Figure 7. Interaction of Beta-Integrin with Talin is necessary for PHP**

**A**) Diagram of *talin* mutations. **B)** Western blot of Talin$^{GFP}$ or Talin$^{GFP\ IBS}$ (Anti-GFP) and Mys (Anti-Mys, Ab CF.6G11) protein from immunoprecipitation of Mew$^{FLAG}$. Beta Tubulin was used as a loading control (anti-beta-Tubulin, Ab AA12.1). Quantification of Talin$^{GFP\ WT}$ or Talin$^{GFP\ IBS}$ protein immunoprecipitation. **C)** Representative traces for indicated genotypes (±PhTx) 60 Hz stimulation. Average EPSC amplitudes normalized to the first pulse are plotted against stimulus number for indicated genotypes and treatments. **D)** Average mEPSC, cumulative EPSC and normalized data (RRP) (± PhTx). **E)** Amplitude of the fourth EPSC divided by the first EPSC in a train (paired pulse ratio, PPR) for indicated genotypes. Averaged data represent mean ± SEM. Significance determined by

One-way Anova with Tukey correction for multiple comparisons. Student's t-test used in graphs containing only two bars; $*p < 0.05$, $**p < 0.01$, $***p < 0.001$. n.s., not significant. Recordings at 1.5 mM $[Ca2+]_e$. Refer to Supplemental Figure 7 for non-normalized RRP data.

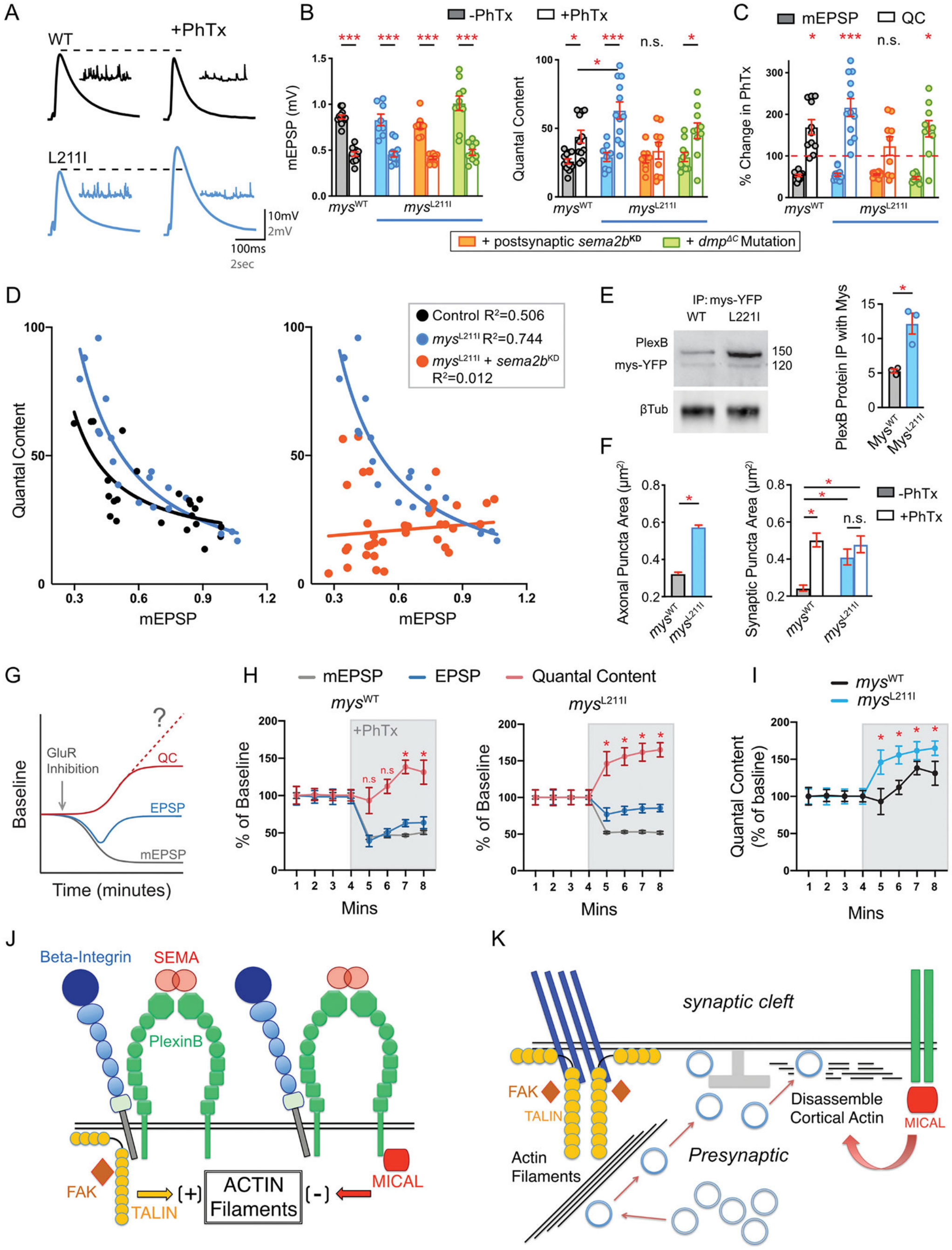

**Figure 8. Activated Beta-Integrin bypasses matrix requirement and accelerates PHP**

**A)** Representative traces (±PhTx). **B)** Averaged mEPSP and quantal content (±PhTx). Genotypes are as follows: $mys^{WT}$ indicates $Ubi{:}mys^{WT\text{-}YFP}$ (black), $mys^{L211I}$ indicates $Ubi{:}mys^{L211I\text{-}YFP}$ (blue), double mutants harboring $Ubi{:}mys^{L211I\text{-}YFP}$ (indicated as horizontal blue line) combined with either *sema2b* knockdown (orange) or a *dmp* mutation (green) (genotypes also indicated with boxes below graph). Genotype naming persist throughout the figure. **C)** Normalized data (± PhTx) with genotypes as in (B). **D)** Each data point represents a single NMJ recording for indicated genotypes. Best fit for data is shown. Equation for each line of best fit as follows: *mys*$^{WT}$ Y= −47.5*X+66.3; *mys*$^{L211I}$ Y= −90.8*X+104.6; *mys*$^{L211I}$, *SemaKD* Y= 6.9*X+19.3. **E)** Western blot of PlexinB$^{FLAG}$ endogenous protein trap (Anti-FLAG, 150kD) and Mys$^{WT\text{-}YFP}$ or Mys$^{L211I\text{-}YFP}$ (Anti-GFP N86/ 8, 120kD) protein from immunoprecipitation of Mys$^{WT\text{-}YFP}$ or Mys$^{L211I\text{-}YFP}$ (Anti-GFP 3E6). Beta Tubulin is loading control. Quantification at right. **F)** Left graph shows data for proximity ligation assay (PLA) of PlexB$^{Myc}$ with Mys$^{WT\text{-}YFP}$ or Mys$^{L211I\text{-}YFP}$. Right graph shown change in Mys$^{WT\text{-}YFP}$ or Mys$^{L211I\text{-}YFP}$ synaptic puncta (±PhTx). **G)** Summary diagram for expectation (Frank et al., 2006) regarding mEPSP, EPSP, and QC after application of sub-blocking PhTx (GluR Inhibition arrow). The mechanism for limiting a homeostatic change in QC remains unknown (dotted line, question mark). **H)** Normalized data for continuous recordings of indicated genotypes. 10 NMJs were recorded from 10 animals per genotype. **I)** Normalized quantal content data for data in (H). Averaged data represent mean ± SEM. Significance determined by One-way Anova with Tukey correction for multiple comparisons: *p < 0.05, **p < 0.01, ***p < 0.001. n.s., not significant. Recordings at 0.3 mM $[Ca^{2+}]_e$. Refer to Supplemental Figure 7 for non-normalized data. **J)** Model. Oligomerization of presynaptic complex including activated beta-Integrin (blue) and activated PlexB (green) in the presence of Sema2b dimers (red ovals). Opposing actions of Talin and MICAL on actin filaments are indicated. **K)** Model. Activity of beta-Integrin (blue) and PlexB (green) are separated (left and right respectively) for clarity. Talin extends into presynaptic cytoplasmic volume, acting to promote a filamentous actin pool that facilitates vesicle recruitment to the RRP. MICAL promotes disassembly of a cortical actin pool, facilitating vesicle fusion. The combined activity is proposed to achieve a regulated and sustained homeostatic increase in the RRP. Refer to Supplemental Figure 7 for non-normalized data.

## KEY RESOURCES TABLE

| REAGENT or RESOURCE | SOURCE | IDENTIFIER |
|---|---|---|
| Antibodies | | |
| mouse anti-Bruchpilot (1:100) | Developmental Studies Hybridoma Bank | Cat# nc82 RRID: AB_2314866 |
| mouse anti-Integrin betaPS (1:10) | Developmental Studies Hybridoma Bank | Cat# cf.6g11 RRID: AB_528310 |
| rabbit anti-Discs large (1:1,000) | Davis lab | N/A |
| mouse anti-ITGb1 AIIB2 (1:100) | Developmental Studies Hybridoma Bank | Cat# aiib2 RRID: AB_528306 |
| mouse anti-ITGb1 9EG7 (1:1000) | BD Pharmingen™ | Cat# 553715 RRID: AB_395001 |
| mouse anti-Talin A22A(1:100) | Developmental Studies Hybridoma Bank | Cat# Talin A22A RRID: AB_10660289 |
| mouse anti-Talin E16B (1:100) | Developmental Studies Hybridoma Bank | Cat# Talin E16B RRID: AB_10683995 |
| mouse anti-Bassoon (1:500) | Fisher Scientific | Cat# ADI-VAM-PS003 RRID: AB_10618753 |
| Aves anti-Neurofilament-H (1:1000) | Aves Labbs,INC. | Cat# NFH RRID: AB_2313552 |
| Alexa secondary anti-mouse-488 (1:500) | Jackson Immuno-research Laboratories | RRID: AB_2338965 Cat#: 115-545-003 |
| Alexa anti-mouse-Cy3 (1:500) | Jackson Immuno-research Laboratories | RRID: AB_2338680 Cat#: 115-165-003 |
| Alexa anti-mouse-Cy5 (1:500) | Jackson Immuno-research Laboratories | RRID: AB_2338714 Cat#: 115-175-166 |
| Alexa anti-rabbit-488 (1:500) | Jackson Immuno-research Laboratories | RRID: AB_2338046 Cat#: 111-545-003 |
| Alexa anti-rabbit-Cy3 (1:500) | Jackson Immuno-research Laboratories | RRID: AB_2338000 Cat#: 111-165-003 |
| Alexa anti-rabbit-Cy5 (1:500) | Jackson Immuno-research Laboratories | RRID:AB_2338013 Cat#: 111-175-144 |
| Alexa anti-chicken-488 (1:500) | Jackson Immuno-research Laboratories | RRID: AB_2337390 Cat#: 103-545-155 |
| Alexa anti-chicken-AlexaFluor-647 (1:500) | Jackson Immuno-research Laboratories | RRID: AB_2337392 Cat#: 103-605-155 |
| mouse anti-GFP 3E6 (1:500) | Life Technologies | Cat# A-11120 RRID: AB_221568 |
| mouse anti-FLAG M2 (1:500) | Sigma-Aldrich | Cat# F1804 RRID: AB_262044 |
| mouse anti-GFP N86/8 (1:10) | UC Davis/NIH Neuro Mab Facility | Cat# N86/8 RRID: AB_10671444 |
| Anti-beta-tubulin AA12. (1:200) | Developmental Studies Hybridoma Bank | Cat# AA12.1 RRID: AB_579794 |
| Anti-actin JLA20 (1:500) | Developmental Studies Hybridoma Bank | Cat# jla20 RRID:AB_528068 |
| rabbit Anti-c-Myc (1:1000) | Sigma-Aldrich | Cat# C3956 RRID: AB_439680 |
| mouse Anti-c-Myc 9E 10 (1:500) | Developmental Studies Hybridoma Bank | Cat# 9E 10 RRID: AB_2266850 |
| Mouse Anti-V5 (1:1000) | Life technologies | RRID: AB_2792973 Cat#: R960CUS |
| Anti-peroxidase Alexa Fluor™ 488 (1:100) | Jackson Immuno-research Laboratories | RRID: AB_2338965 Cat#: 123-545-021 |

| **REAGENT or RESOURCE** | **SOURCE** | **IDENTIFIER** |
|---|---|---|
| Anti-peroxidase Cy3 (1:100) | Jackson Immuno-research Laboratories | RRID: AB_2338959 Cat#: 123-165-021 |
| Anti-peroxidase Alexa Fluor™ 647 (1:100) | Jackson Immuno-research Laboratories | RRID: AB_2338967 Cat#: 123-605-021 |
| α-Bungarotoxin, Alexa Fluor™ 647 (1:500) | Thermo Fisher Scientific | Cat#: B35450 |
| α-Bungarotoxin, Alexa Fluor™ 555 (1:500) | Thermo Fisher Scientific | Cat#: B35451 |
| Chemicals, Peptides, and Recombinant Proteins | | |
| Philanthotoxin-433 | Santa Cruz Biotechnology | Cat#: 276684-27-6 |
| M 4-(4-diethylaminostyryl)-N-methylpyridinium iodide | Invitrogen | Cat#: D288 |
| conotoxin GIIIB | Peptide Institute, Inc. | Cat#: 4217-v |
| D-Tubocurarine | Sigma Aldrich | Cat#: T2379 |
| RGD Peptide | Abbiotec, Inc. | Cat#: 350362 |
| Critical commercial assays | | |
| Duolink® In Situ Red Starter Kit Mouse/Rabbit | MilliporeSigma | Cat#: DUO92101 |
| Experimental Models: Organisms/Strains | | |
| *D. melanogaster w*$^{\textit{1118}}$ | Bloomington Stock Center | Stock#: BL19062 |
| *D. melanogaster mys*$^{\textit{1}}$ | Bloomington Stock Center | Stock#: BL59 |
| *D. melanogaster mys*$^{\textit{b8}}$ | Gift from Dr.Guy Tanentzapf | (Jannuzi, A.L.,et al., 2004) |
| *D. melanogaster mys*$^{\textit{42}}$ | Gift from Dr.Guy Tanentzapf | (Jannuzi, A.L.,et al., 2004) |
| *D. melanogaster mys*$^{\textit{GFP}}$ | Davis Lab | Generated for this project |
| *D. melanogaster mys*$^{\textit{Ubi-p63E.Venus}}$ | Gift from Dr.Guy Tanentzapf | (Yuan, et al., 2010) |
| *D. melanogaster mys*$^{\textit{L211I.EYFP.Ubi-p63E}}$ | Gift from Dr.Guy Tanentzapf | (Pines, et al., 2011) |
| *D. melanogaster mys*$^{\textit{G792N.EYFP.Ubi-p63E}}$ | Gift from Dr.Guy Tanentzapf | (Pines, et al., 2011) |
| *D. melanogaster mys*$^{\textit{D807R.EYFP.Ubi-p63E}}$ | Gift from Dr.Guy Tanentzapf | (Pines, et al., 2011) |
| *D. melanogaster mys*$^{\textit{L796R.EYFP.Ubi-p63E}}$ | Gift from Dr.Guy Tanentzapf | (Pines, et al., 2011) |
| *D. melanogaster mys*$^{\textit{804stop.EYFP.Ubi-p63E}}$ | Gift from Dr.Guy Tanentzapf | (Pines, et al., 2011) |
| *D. melanogaster mys*$^{\textit{S196F.EYFP.Ubi-p63E}}$ | Gift from Dr.Guy Tanentzapf | (Pines, et al., 2011) |
| *D. melanogaster mys*$^{\textit{N840A.EYFP.Ubi-p63E}}$ | Gift from Dr.Guy Tanentzapf | (Pines, et al., 2011) |
| *D. melanogaster mys*$^{\textit{N840A GFP}}$ | Davis Lab | Generated for this project |
| *D. melanogaster mys*$^{\textit{S196F GFP}}$ | Davis Lab | Generated for this project |
| *D. melanogaster UAS-FLAG-Mys* | Gift from Jan Lab | (Meltzer, S. et al., 2016) |
| *D. melanogaster Mew*$^{\textit{FLAG}}$ | Kyoto Stock Center | Stock#: 115524 |
| *D. melanogaster Mew RNAi P{TRiP.JF02694}attP2* | Bloomington Stock Center | Stock#: BL 27543 |
| *D. melanogaster UAS-Myc-PlexB* | Gift from Dr Yuh-Nung Jan | (Meltzer, S et al., 2016) |
| *D. melanogaster plexBKG00878* | Gift from Dr Yuh-Nung Jan | (Ayoob et al., 2006) |
| *D. melanogaster UAS-PlexB V5* | Gift from Dr Liqun Luo | (Guajardo, R et all., 2019) |
| *D. melanogaster UAS-PlexB*$^{\Delta\textit{sema}}$*V5* | Gift from Dr Liqun Luo | (Guajardo, R et all., 2019) |
| *D. melanogaster plexB*$^{\textit{FLAG}}$ | Gift from Dr Liqun Luo | (Li, J. et al., 2018) |
| *D. melanogaster Talin*$^{\textit{BFPMyc}}$ | This paper | N/A |

| **REAGENT or RESOURCE** | **SOURCE** | **IDENTIFIER** |
|---|---|---|
| *D. melanogaster Talin*$^{Ubi\text{-}p63E.EGFP}$ | Gift from Dr.Guy Tanentzapf | (Yuan, et al., 2010) |
| *D. melanogaster Talin* $^{R367A.LI.AA.Ubi\text{-}p63E.EGFP}$ | Gift from Dr.Guy Tanentzapf | (Ellis et al., 2011) |
| *D. melanogaster Talin RNAi P{TRiP.HM05161}attP2* | Bloomington Stock Center | Stock#: BL28950 |
| *D. melanogaster P{SUPor-P}Fak* $^{KG00304}$ | Bloomington Stock Center | Stock#: BL13080 |
| *D. melanogaster Fak RNAi P{TRiP.JF02484}attP2* | Bloomington Stock Center | Stock#: BL29323 |
| *D. melanogaster Fak RNAi P{TRiP.HMS00010}attP2* | Bloomington Stock Center | Stock#: BL33617 |
| *D. melanogaster P{GawB}VGlut[OK371]* | Bloomington Stock Center | Stock#: BL26160 |
| *D. melanogaster P{GawB}C57* | Gift from Dr. Vivian Budnik | N/A |
| *M. musculus Hb9* $^{cre}$ | Jackson Lab | Stock#: 006600 |
| *M. musculus Itgb1* $^{tm1Efu}$ | Jackson Lab | Stock#: 004605 |
| Oligonucleotides | | |
| *Mys*$^{GFP}$ (*Drosophila knock-in*) Mutant forward 5’-GGAGCGCATGAACGCCAAGT-3’ | This paper | N/A |
| *Mys*$^{GFP}$ (*Drosophila knock-in*) Mutant reverse 3’-ACTTCAGTGGTTTTGCACCC-5’ | This paper | N/A |
| *mys*$^{N840A\ GFP}$ (*Drosophila knock-in*) Mutant forward 5’-GGAGCGCATGAACGCCAAGT-3’ | This paper | N/A |
| *mys*$^{N840A\ GFP}$ (*Drosophila knock-in*) Mutant reverse 3’-ACTTCAGTGGTTTTGCACCC-5’ | This paper | N/A |
| *mys*$^{S196F\ GFP}$ (*Drosophila knock-in*) Mutant forward 5’-AAATATAAGTGAACCAGGAA-3’ | This paper | N/A |
| *mys*$^{S196F\ GFP}$ (*Drosophila*) Mutant reverse 3’-CTTGCTAACTGTAGAACGAA -5’ | This paper | N/A |
| Software and Algorithms | | |
| GraphPad Prism (9) | GraphPad | https://www.graphpad.com/scientific-software/prism/ |
| MiniAnalysis (6.0.3) | Synaptosoft | N/A |
| Igor Pro (8) | WaveMetrics | https://www.wavemetrics.com |
| Fiji | NIH | https://ImageJ.NIH.gov/IJ |
| SlideBook 6 | Intelligent Imaging Innovation | https://www.intelligent-imaging.com |